CDF note XXXX

Measurement of Z/γ^* + jets differential cross sections in $\mathrm{p\bar{p}}$ collisions at $\sqrt{s} = 1.96$ TeV

The CDF Collaboration[1]

[1] *URL http://www-cdf.fnal.gov*

(Dated: February 20, 2014)

Abstract

Differential Z/γ^* + jets production cross sections in $\mathrm{p\bar{p}}$ collisions at $\sqrt{s} = 1.96$ TeV are measured with the full data sample collected with the CDF detector in Tevatron Run II, corresponding to 9.6 fb^{-1} of integrated luminosity. Results include first measurements at CDF of differential cross sections in events with a Z/γ^* and 3 or more jets, the inclusive cross section of $Z/\gamma^* + \geqslant 4$ jets production, and various angular observables in the lower jet multiplicity final states. Measured cross sections are compared to several theoretical predictions, among which are perturbative QCD predictions at next-to-leading order (NLO) and approximate next-to-next-to-leading order (NNLO), predictions from event generators based on leading order (LO) and NLO matrix elements matched to parton showers, and perturbative NLO QCD predictions including NLO electro-weak corrections.

I. INTRODUCTION

Studies of the production of jets in association with a Z boson are central to the hadron colliders physics program. Differential cross section measurements provide means to stringently test perturbative QCD predictions [1]. In addition, $Z/\gamma^* +$ jets production is a background to many rare standard model (SM) processes and searches for new physics. Dedicated measurements help to improve the $Z/\gamma^* +$ jets theoretical modelling which is of high relevance in the context of searches and measurement of rare processes, such as the Higgs boson.

Differential cross sections have been previously measured by the CDF [2] and D0 [3] collaborations as a function of several variables, including the jet transverse momentum, the jet rapidity and various angular observables. These measurements are in reasonable agreement with next-to-leading order (NLO) perturbative QCD predictions but are statistically limited in the high jet multiplicity bins. Recently, measurements have also been pursued by the ATLAS [4] and CMS [5] collaborations, since the understanding of these SM processes is essential in the search for new physics at the LHC.

In this article, measurements of differential cross sections for Z/γ^* + jets production are presented, using the full data sample collected with the CDF detector in Run II of the Tevatron Collider, which corresponds to 9.6 fb^{-1}. The results include differential cross sections as a function of transverse momentum p_{T} and rapidity y of jets [6], extended for the first time at CDF to the $Z/\gamma^* + \geqslant 3$ jets final state, the total cross section as a function of jet multiplicity up to four jets, and several differential distributions for events with a Z/γ^* and at least one or two jets. Measurements are compared to NLO [7, 8] and approximate NNLO perturbative QCD predictions [9], to NLO QCD predictions including NLO electro-weak corrections [10], and to distributions from various fixed order plus parton shower Monte Carlo generators [11, 12].

This paper is organized as follows: Section II contains a brief description of the CDF detector, and the data sample and the event selection are presented in Section III. The Monte Carlo samples used across the analysis are listed in Section IV and the estimation of the background contributions is described in Section V. The unfolding procedure is explained in Section VI and the systematic uncertainties are addressed in Section VII. The theoretical predictions are described in Section VIII and the measured differential cross sections are shown and discussed in Section IX. Section X summarizes the results.

II. THE CDF II DETECTOR

The CDF II detector, described in detail in [13], is composed of a precision tracking system embedded in a 1.4 T magnetic field and surrounded by electromagnetic and hadronic calorimeters and muon spectrometers. CDF uses a cylindrical coordinate system in which the z axis lies along the proton beam direction, ϕ is the azimuthal angle and θ is the polar angle, which is often expressed as pseudo-rapidity $\eta = -\ln(\tan(\theta/2))$. The tracking system consists of a silicon micro-strip detector covering a pseudo-rapidity range of $|\eta| < 2$ and provides precise three-dimensional track reconstruction. The silicon detector is surrounded by a 3.1 m long open-cell drift chamber (COT) which covers a pseudo-rapidity range of $|\eta| < 1$ and measures precisely the momentum of charged particles. The COT sits inside the 1.4 T superconducting solenoidal magnet which is surrounded by the calorimeter system. This system, arranged in a projective tower geometry, measures particle energies for $|\eta| < 3.6$. The electromagnetic calorimeter is a lead-scintillator sampling calorimeter which also contains proportional chambers and resistive strips at a depth corresponding to the maximum shower intensity for electrons. The hadronic calorimeter is an iron-scintillator sampling calorimeter. The muon detectors, located outside the calorimeters, consist of drift chambers and scintillation counters covering a pseudo-rapidity range of $|\eta| < 1.0$. Finally, the luminosity is computed via the number of inelastic $p\bar{p}$ collisions determined by the Cherenkov counters located close to the beam pipe.

III. DATA SAMPLE AND EVENT SELECTION

The data sample consists of $Z/\gamma^*(\rightarrow e^+e^-)$ and $Z/\gamma^*(\rightarrow \mu^+\mu^-)$ + jets candidate events which have been collected using a three-level online event selection system [14] between February 2002 and September 2011. In the electron channel, the online event selection requires a central ($|\eta| < 1$) electromagnetic calorimeter cluster with $E_T > 18$ GeV matched to a track of $p_T > 9$ GeV/c. Offline, $Z/\gamma^*(\rightarrow e^+e^-)$ events are selected if two central electrons of $E_T > 25$ GeV are identified and reconstructed with an invariant mass in the range $66 < M_{ee} < 116$ GeV/c^2. Details on the electron identification requirements are given in Ref. [13]. In the muon channel, the online event selection requires a signal in the muon detectors associated to a track reconstructed in the drift chamber with $|\eta| < 1$ and $p_T > 18$ GeV/c. Offline, $Z/\gamma^*(\rightarrow \mu^+\mu^-)$ events are required to have two reconstructed opposite signed muons each with $|\eta| < 1$, $p_T > 25$ GeV/c and $66 < M_{\mu\mu} <$

116 GeV/c^2. Quality requirements are applied to the track in order to reject misidentified muons, and all the muon candidates are required to have deposited energy in the calorimeter consistent with a minimum ionizing particle. More details on the muon reconstruction and identification can be found in Ref. [13].

In addition to a Z boson candidate, one or more jets with $p_{\mathrm{T}} > 30$ GeV/c and rapidity $|y| < 2.1$ are required. Jets are reconstructed using the midpoint algorithm [15] in a cone of radius $R = 0.7$ [16] and a merging/splitting fraction of 0.75. Calorimeter towers are clustered if the energy deposits correspond to a transverse energy greater than 0.1 GeV [17] and used as seeds if larger than 1 GeV. Towers associated with reconstructed electrons and muons are excluded. Jet 4-momenta are evaluated by combining the 4-momenta of the towers according to the E-scheme: $p^{\mu}_{\mathrm{jet}} = \sum p^{\mu}_{\mathrm{towers}}$ [18]. With such a recombination scheme, jets are in general massive, and in order to study the jet kinematics, the variables $p_{\mathrm{T}}^{\mathrm{jet}}$ and y^{jet} are used, which account for the jet mass. Since the measured jet transverse momentum, $p_{\mathrm{T,cal}}^{\mathrm{jet}}$ (calorimeter level), is affected by instrumental effects, an average correction [19] is applied to $p_{\mathrm{T,cal}}^{\mathrm{jet}}$. This effect, mainly due to the non-compensating nature of the calorimeter and the presence of inactive material, is of the order of 30% for $p_{\mathrm{T,cal}}^{\mathrm{jet}}$ around 40 GeV/c and reduces to about 11% for high $p_{\mathrm{T,cal}}^{\mathrm{jet}}$ jets. A further correction is applied to account for the energy contributions to jets from multiple $\mathrm{p\bar{p}}$ interactions but no modification is done to account for underlying event contributions or fragmentation effects. The requirement of $p_{\mathrm{T}} > 30$ GeV/c is applied to the corrected jet transverse momentum. Events are selected if the leptons are separated from the selected jets by $\Delta R_{\mathrm{lepton-jet}} > 0.7$ [20].

IV. MONTE CARLO SIMULATION

Samples of Z/γ^* + jets events are generated using ALPGEN v2.14 [11] interfaced to PYTHIA 6.4.25 [21] for the parton showering, with CTEQ5L as parton distribution functions (PDF) [22] and using the set of *tuning* parameters denoted as Tune Perugia 2011 [23]. The MLM matching procedure [24] is applied to avoid double-counting between the matrix-element calculations and the parton showering algorithm of PYTHIA. In addition, samples for background processes and inclusive Z/γ^* production are generated using PYTHIA v6.2 with the same PDF set and Tune A [25]. All the samples are passed through a full CDF detector simulation based on GEANT [26] where the GFLASH [27] package is used for parametrization of the energy deposition in the calorimeters, and corrected to account for differences between data and simulation in the online event selection and lepton identification efficiencies. The electron E_T and the muon p_T scale and resolution are corrected to match the dilepton invariant mass distributions observed in the data in the region $84 < M_{ll} < 98$. The Z/γ^* + jets samples are also reweighted in the number of multiple $\mathrm{p\bar{p}}$ interactions in the same bunch crossing so as to have the same instantaneous luminosity profile of the data. The Monte Carlo samples are used to determine background contributions and to derive the unfolding correction factors described in Section VI.

V. BACKGROUNDS CONTRIBUTIONS

Various strategies are used to estimate the background contributions. In the $Z/\gamma^*(\to e^+e^-)$ channel, one of the largest contribution comes from inclusive jets and W + jets events in which one or more jets are misidentified as electrons; a data-driven method is used to estimate this source of background. First, the probability for a jet to pass the electron selection requirements is evaluated using an inclusive jet data sample. This is denoted as a *fake* probability and is parametrized as a function of the jet transverse energy, corrected to match on average the corresponding electron energy, and applied to jets from a sample of events with one reconstructed electron. For each event, all the possible electron-jet combinations are considered as Z/γ^* candidates, and all the electron-jet pairs that fulfill the analysis event selection requirements are weighted with the corresponding fake probability associated to the jet and used to estimate the background rate for each measured distribution.

In the muon channel the W + jets and inclusive jets processes constitute a source of background when a track inside a jet is identified as a muon. To estimate this background contribution, events containing muon pairs are reconstructed following the analysis selection but requiring the charge of the two muons to have the same sign.

Other background contributions are estimated with Monte Carlo samples, and can originate from $t\bar{t}$, associated production of W and Z bosons (WW, WZ, ZZ) and $Z/\gamma^*(\to \tau^+\tau^-)$ + jets. The $t\bar{t}$ sample is normalized according to the approximate NNLO cross section [28], the WW, WZ and ZZ samples are normalized according to the NLO cross section [29], and the $Z/\gamma^*(\to \tau^+\tau^-)$ + jets sample is normalized according to the Z inclusive NNLO cross section [13]. The total background varies from about 2% to 6% depending on the jet multiplicity as shown in Table I, which reports the sample composition per jet multiplicity bin in the electron and muon channels.

Figure 1 shows the invariant mass distribution for $Z/\gamma^* + \geqslant 1$ jet events in the electron and

TABLE I. Estimated background contributions, background systematic uncertainties and data yield for (a) $Z/\gamma^*(\rightarrow e^+e^-)+\geqslant N_{\text{jet}}$ and (b) $Z/\gamma^*(\rightarrow \mu^+\mu^-)+\geqslant N_{\text{jet}}$, with $N_{\text{jet}} = 1,2,3$, and 4.

$Z/\gamma^*(\rightarrow e^+e^-)$ + jets	Estimated events in 9.4 fb^{-1}			
Backgrounds	$\geqslant$ 1 jet	$\geqslant$ 2 jets	$\geqslant$ 3 jets	$\geqslant$ 4 jets
QCD, W + jets	25.9 ± 3.9	4.0 ± 0.6	0.6 ± 0.1	0.1 ± 0.0
WW, ZZ, ZW	119 ± 36	43 ± 13	4.2 ± 1.3	0.3 ± 0.1
$t\bar{t}$	45 ± 13	25.4 ± 7.6	2.9 ± 0.9	0.2 ± 0.1
$Z/\gamma^*(\rightarrow \tau^+\tau^-)$ + jets	7.2 ± 2.2	0.5 ± 0.1	0.0 ± 0.0	0.0 ± 0.0
Total Background	197 ± 38	73 ± 15	7.8 ± 1.5	0.7 ± 0.1
Data	12910	1451	137	13

(a)

$Z/\gamma^*(\rightarrow \mu^+\mu^-)$ + jets	Estimated events in 9.6 fb^{-1}			
Backgrounds	$\geqslant$ 1 jet	$\geqslant$ 2 jets	$\geqslant$ 3 jets	$\geqslant$ 4 jets
QCD, W + jets	51 ± 51	18 ± 18	3 ± 3	1 ± 1
WW, ZZ, ZW	190 ± 57	69 ± 21	6.7 ± 2.0	0.5 ± 0.2
$t\bar{t}$	68 ± 21	38 ± 12	4.5 ± 1.3	0.5 ± 0.1
$Z/\gamma^*(\rightarrow \tau^+\tau^-)$ + jets	9.4 ± 2.8	1.2 ± 0.3	0.1 ± 0.0	0.0 ± 0.0
Total Background	318 ± 79	126 ± 30	14.3 ± 3.8	2.0 ± 1.0
Data	19578	2247	196	13

(b)

muon decay channels. The region outside the mass window used in the analysis contains a larger fraction of background processes. Table II shows the comparison between data and Z/γ^* + jets signal plus background prediction for $Z/\gamma^*+\geqslant 1$ jet events in the low and high mass regions $40 < M_{ll} < 66$ GeV/c^2 and $116 < M_{ll} < 145$ GeV/c^2. The good agreement between data and expectation validates the background contribution estimation.

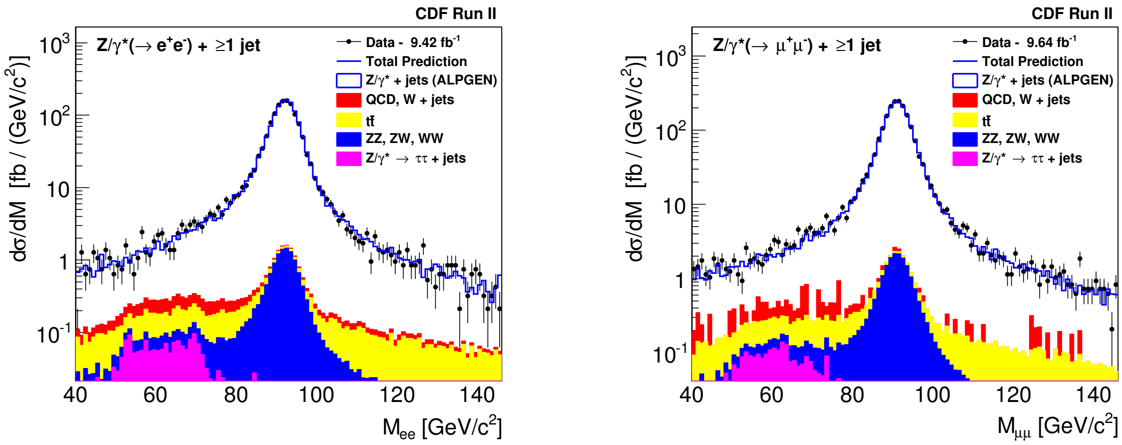

(a) (b)

FIG. 1. Dilepton invariant mass for events with at least one jet in the (a) $Z/\gamma^*(\rightarrow e^+e^-)$ and (b) $Z/\gamma^*(\rightarrow \mu^+\mu^-)$ channels. Observed events divided by the integrated luminosity (black dots) are compared to the Monte Carlo expectation (blue line), including signal and backgrounds contributions (filled histograms).

TABLE II. Estimated background events and Z/γ^* + jets Monte Carlo prediction compared to the data yield in the low and high regions outside the mass window used in the analysis, for $Z/\gamma^*(\rightarrow e^+e^-)+\geqslant 1$ jet and $Z/\gamma^*(\rightarrow \mu^+\mu^-)+\geqslant 1$ jet events. Invariant mass ranges are given in GeV/c^2. Background systematic uncertainties and the statistical uncertainties of the Z/γ^* + jets Monte Carlo prediction are shown

	$Z/\gamma^*(\rightarrow e^+e^-)+\geq 1$ jet		$Z/\gamma^*(\rightarrow \mu^+\mu^-)+\geq 1$ jet	
Backgrounds	$40 < M_{ee} < 66$	$116 < M_{ee} < 145$	$40 < M_{\mu\mu} < 66$	$116 < M_{\mu\mu} < 145$
QCD, W + jets	15.9 ± 2.4	2.9 ± 0.4	37 ± 37	8 ± 8
WW, ZZ, ZW	5.2 ± 1.6	3.2 ± 1.0	7.5 ± 2.3	4.6 ± 1.4
$t\bar{t}$	19.7 ± 5.9	15.6 ± 4.7	30.1 ± 9.0	22.4 ± 6.7
$Z/\gamma^*(\rightarrow \tau^+\tau^-)$ + jets	10.9 ± 3.3	0.3 ± 0.1	17.5 ± 5.2	0.3 ± 0.1
Total Background	51.7 ± 7.3	21.9 ± 4.8	92 ± 39	35 ± 11
Z/γ^* + jets (ALPGEN)	238.6 ± 6.5	196.7 ± 5.6	335.4 ± 7.2	289.0 ± 6.4
Total prediction	290.3 ± 9.8	218.6 ± 7.3	428 ± 39	324 ± 12
Data	312	226	486	334

VI. UNFOLDING

Measured cross sections need to be corrected for detector effects in order to be compared to the theoretical predictions. The comparison between data and predictions is performed at the particle level, which refers to physics objects reconstructed from quasi-stable (lifetime > 10 ps) and confined final state particles including hadronization and underlying event contribution, but not the contribution of multiple $p\bar{p}$ interactions in the same bunch crossing [30]. Detector-level cross sections are calculated by subtracting the estimated background from the observed events in each bin and dividing by the integrated luminosity. Measured cross sections are unfolded from detector-level to particle level with a bin-by-bin procedure. For each bin of a measured observable α, the ALPGEN+PYTHIA $Z/\gamma^{*}(\rightarrow e^{+}e^{-})$ + jets and $Z/\gamma^{*}(\rightarrow \mu^{+}\mu^{-})$ + jets Monte Carlo samples are used to evaluate the unfolding factors, which are defined as $U_{\alpha} = \frac{d\sigma^{\mathrm{MC}}}{d\alpha^{\mathrm{detector}}} / \frac{d\sigma^{\mathrm{MC}}}{d\alpha^{\mathrm{particle}}}$. Particle level cross sections are evaluated as $\frac{d\sigma}{d\alpha^{\mathrm{particle}}} = \frac{d\sigma}{d\alpha^{\mathrm{detector}}} \cdot U_{\alpha}$. The Monte Carlo samples used for the unfolding are validated by comparing measured and predicted cross sections at detector level. The unfolding factors account for $Z/\gamma^{*}(\rightarrow l^{+}l^{-})$ reconstruction efficiency, particle detection and jet reconstruction in the calorimeter. Unfolding factors are typically around 1.7 (2.5) in value and vary between 1.6 (2.3) at low p_{T} and 2 (3) at high p_{T} for the $Z/\gamma^{*}(\rightarrow \mu^{+}\mu^{-})$ ($Z/\gamma^{*}(\rightarrow e^{+}e^{-})$) channel.

At particle level, radiated photons are recombined with leptons following a scheme similar to that used in [10]. A photon and a lepton from $Z/\gamma^{*}(\rightarrow l^{+}l^{-})$ decay are recombined when $\Delta R_{\gamma-l} < 0.1$. If both charged leptons in the final state are close to a photon, the photon is recombined with the lepton with the smallest $\Delta R_{\gamma-l}$. Photons which are not recombined to leptons are included in the list of particles for the jet clustering. With such a definition, photons can be clustered into jets at the particle level, and Z/γ^{*} + γ production is included in the definition of Z/γ^{*} + jets. The contribution of Z/γ^{*} + γ process to the Z/γ^{*} + jets cross section is at the percent level, and accounted in the PYTHIA simulation through photon initial state radiation (ISR) and final state radiation (FSR).

Physics object reconstruction and kinematic requirements applied at particle level establish the measurement definition. Requirements applied at the detector level are also applied to jets and leptons at the particle level so as to reduce the uncertainty of the extrapolation of the measured cross section. Jets are reconstructed at particle level in the Monte Carlo sample with the midpoint algorithm in a cone of radius $R = 0.7$, the merging/splitting fraction set to $f = 0.75$, and using

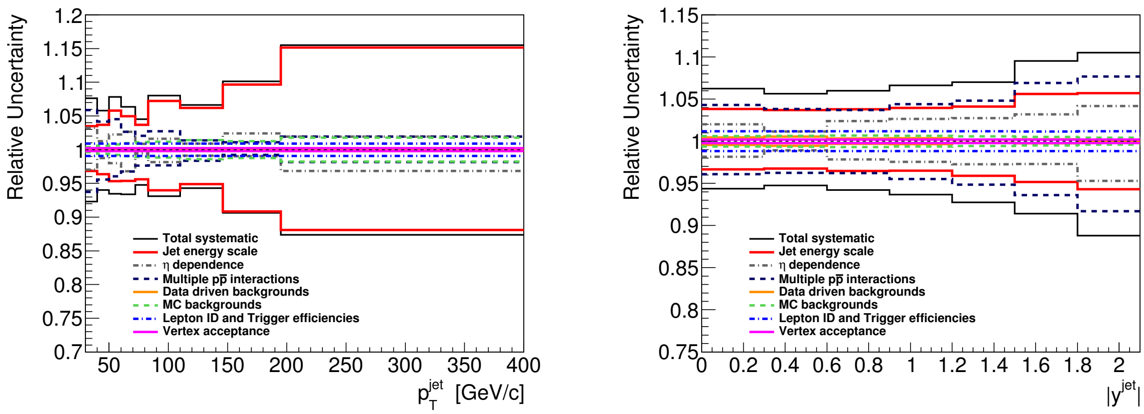

(a) (b)

FIG. 2. Systematic uncertainties as a function of (a) inclusive jet p_{T} and (b) inclusive jet rapidity (right) in events with $Z/\gamma^{*}+\geqslant 1$ jet.

as seeds particles with $p_{\mathrm{T}} \geqslant 1$ GeV/c. The measured cross sections are defined in the kinematic region $66 < M_{ll} < 116$ GeV/c^2, $|\eta^{l}| < 1$, $p_{\mathrm{T}}^{l} > 25$ GeV/c ($l = e,\ \mu$), $p_{\mathrm{T}}^{\mathrm{jet}} > 30$ GeV/c, $|y^{\mathrm{jet}}| < 2.1$, and $\Delta R_{\mathrm{lepton-jet}} > 0.7$.

VII. SYSTEMATIC UNCERTAINTIES

Several sources of systematic uncertainties that affect the measured cross sections have been carefully studied. The main systematic uncertainty of the $Z/\gamma^{*}(\rightarrow l^{+}l^{-})$ + jets measurement is due to the jet energy scale correction. The jet energy scale is varied according to [19] to account for the related systematic uncertainty. Three sources of systematic uncertainty are considered: the absolute jet energy scale, multiple $p\bar{p}$ interactions, and the η-dependent calorimeter response. The absolute jet energy scale uncertainty depends on the response of the calorimeter to an individual particle and on how well the Monte Carlo reproduces the particle multiplicity and p_{T} spectrum inside a jet. This uncertainty significantly affects observables involving high p_{T} jets and high jet multiplicity. The jet energy uncertainty related to multiple $p\bar{p}$ interactions arises from inefficiency in the reconstruction of multiple interactions vertices, and mainly affects low jet p_{T} ($\sim$5%) and high jet rapidity kinematic regions, and high jet multiplicity. The η-dependent uncertainty accounts for residual discrepancies between data and Monte Carlo after the calorimeter response has been corrected for the dependence on η.

Online event selection efficiency and lepton identification uncertainties are of the order of 1% and give small contributions to the total uncertainty.

A conservative 30% uncertainty is assigned to the Monte Carlo backgrounds estimation, to account for missing higher order corrections on the cross sections normalization. In the $Z/\gamma^*(\rightarrow e^+e^-)$ channel, a 15% uncertainty is assigned to the data-driven QCD and W + jets background subtraction, to account for the statistical and systematic uncertainty of the fake rate parametrization. In the $Z/\gamma^*(\rightarrow \mu^+\mu^-)$ channel a 100% uncertainty is applied to the subtraction of QCD and W + jets background, which accounts for any difference between the observed same-sign yield and the expected opposite-sign background contribution. The impact of both sources to the uncertainties of the measured cross sections is less than 2%. The uncertainty on the primary vertex acceptance is ~1%. Finally, the luminosity estimation has an uncertainty of 5.8% which is applied to the measurements [31]. Systematic uncertainties as a function of inclusive jet p_{T} and rapidity are shown in Figure 2.

VIII. THEORETICAL PREDICTIONS

Measured Z/γ^* + jets differential cross sections are compared to several theoretical predictions such as NLO perturbative QCD calculations evaluated with MCFM [7] and BLACKHAT+SHERPA [8], approximate NNLO LOOPSIM+MCFM ($\bar{\text{n}}$NLO) [9] and to generators based on LO matrix element (ME) supplemented by parton showers (PS), like ALPGEN+PYTHIA [11, 21], and NLO ME+PS as POWHEG+PYTHIA [12].

The parameters of the different predictions have been chosen to be homogeneous in order to emphasize the difference between the theoretical models. The MSTW2008 [32] PDF sets have been used as the default choice in all the predictions. LO PDF and 1-loop running order of α_s are used for the LO MCFM and BLACKHAT+SHERPA predictions, NLO PDF and 2-loop running order of α_s for POWHEG, ALPGEN, NLO MCFM and NLO BLACKHAT predictions, and NNLO PDF and 3-loop running order of α_s for the $\bar{\text{n}}$NLO LOOPSIM prediction. The contribution of PDF to the uncertainty of the NLO MCFM prediction is estimated with the MSTW2008NLO 68% confidence level (CL) uncertainty PDF set which are derived using the Hessian method [33]. There are 20 eigenvectors and a pair of uncertainty PDF associated with each eigenvector. The pair of PDF corresponds to positive and negative 68% CL excursions along the eigenvector. The PDF contribution to the prediction uncertainty is the quadrature sum of prediction uncertainties from each uncertainty PDF set. The impact of different PDF sets has been studied in MCFM, ALPGEN and POWHEG. The variation in the predictions with CTEQ6.6 [34], NNPDF2.1 [35], CT10 [36] and MRST2001 [37] PDF sets is of the same order of the MSTW2008NLO uncertainty. The LHAPDF 5.8.6 library [38] has been used to access PDF sets, except in ALPGEN where PDF sets are provided within the Monte Carlo program.

The nominal choice for the functional form of the renormalization and factorization scale is $\mu_0 = \hat{H}_T/2 = \frac{1}{2}\left(\sum_j p_T^j + p_T^{l^+} + p_T^{l^-}\right)$ [39] where the index j runs over the partons in the final state. Such choice is suggested in [40]; and for a further discussion on the appropriate scale for V + jets processes see also [41]. An exception to this default choice is the ALPGEN prediction, where the default scale is set to $\mu_0 = \sqrt{m_Z^2 + \sum_j p_T^j}$; the difference with respect to $\mu_0 = \hat{H}_T/2$ has been studied and found to be negligible. The factorization and renormalization scale has been varied between half and twice the nominal value $\mu_0 = \mu_0/2$, $\mu_0 = 2\mu_0$, and the corresponding variation in the cross sections is considered as an uncertainty of the prediction. This is the largest uncertainty associated to the theoretical models, except for the ALPGEN+PYTHIA prediction, where the largest uncertainty is associated with the variation of the renormalization scale using the CKKW scale-setting procedure [42]. In the ALPGEN prediction, following the prescription of [43], the value of Λ_{QCD} in the CKKW scale setting procedure is set to $\Lambda_{QCD} = 0.26$ and the running order of α_s to 1-loop. These settings match the corresponding values of Λ_{QCD} and the running order of α_s for ISR and FSR of the PYTHIA Tune Perugia 2011. The variation of the CKKW renormalization scale is done together with opposite variation of Λ_{QCD} in the PYTHIA tune. Variations of the renormalization and factorization scale for the matrix element generation is performed independently, and this variation primarily affects the factorization scale because the renormalization scale is later reset in the CKKW procedure. The difference with respect to the previous Tune A and Tune DW have been studied, with the α_s-matched setup of Tune Perugia 2011 providing a better modelling of the shape and normalization of the Z/γ^* + jets differential cross sections. In the case of Tunes A and DW, the running of α_s^{CKKW} in ALPGEN and Λ_{QCD} in PYTHIA are determined by the PDF set, which is CTEQ5L in both ALPGEN and PYTHIA to avoid mismatch. The POWHEG calculation is performed with the weighted events option, and the Born suppression factor for the reweight is set to 10 GeV/c, following the prescription used in [12]. Further studies on the impact of different choices of the functional form of the renormalization and factorization scale have been performed in [44].

In the LO and NLO MCFM predictions, jets are clustered with the native MCFM *cone* algorithm

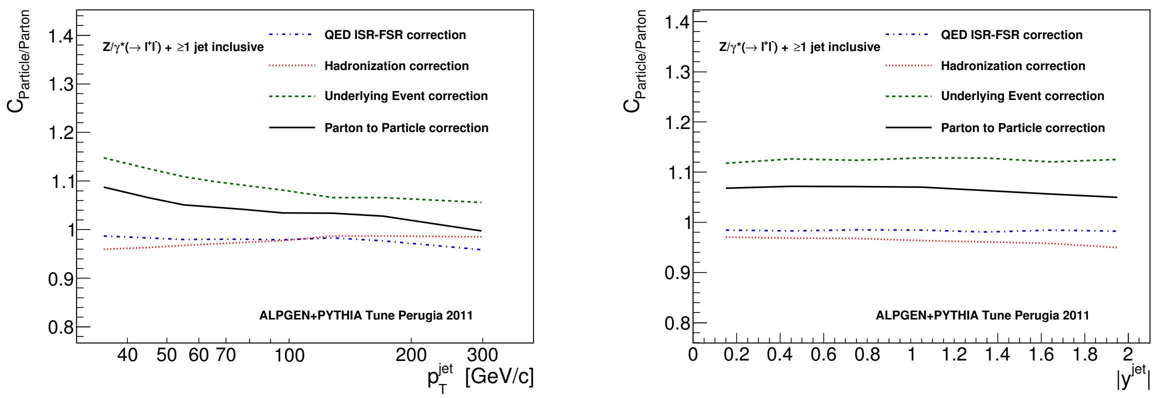

(a) (b)

FIG. 3. Parton to particle corrections as a function of (a) inclusive jet $p_{\rm T}$ and (b) inclusive jet rapidity for Z/γ^{*} + $\geqslant$ 1 jet events. The relative contribution of QED radiation, hadronization and underlying event is shown.

with $R = 0.7$. This algorithm is a seedless cone algorithm which follows the jet clustering outlined in [18]. Parameters of merging fraction f and R_{sep} [45] have been set to $f = 0.75$ and $R_{sep} = 1.3$ following the same prescription used in the previous Z/γ^{*} + jets measurement at CDF [2]. In order to run the LOOPSIM method on top of the MCFM calculation, a different setup has been used. In this case the minimum jet $p_{\rm T}$ for the generation is set to 1 GeV/c, and the jet clustering is performed with the fastjet [46] interface to the SISCone [47] jet algorithm with parameters $R = 0.7$ and $f = 0.75$. The same parameters and setup for the jet clustering have been used in the BLACKHAT+SHERPA calculation, and the predictions were provided by the BLACKHAT authors [48].

A recently developed Monte Carlo program allows the calculation of both NLO electro-weak and NLO QCD corrections to the $Z/\gamma^{*}+\geqslant 1$ jet cross sections [10], the QCD and electro-weak part of the NLO corrections are combined with a factorization ansatz: NLO QCD and electro-weak corrections to the LO cross section are evaluated independently and combined with a multiplicative approach. The NLO QCD $\otimes$ NLO EW prediction is evaluated with the setup described in [10], except for the renormalization and factorization scale which are set to $\mu_0 = \hat{H}_T/2$, and the predictions were provided by the authors [49].

Fixed-order perturbative QCD predictions need to be corrected for non-perturbative QCD effects in order to compare them with the measured cross sections, including the underlying event

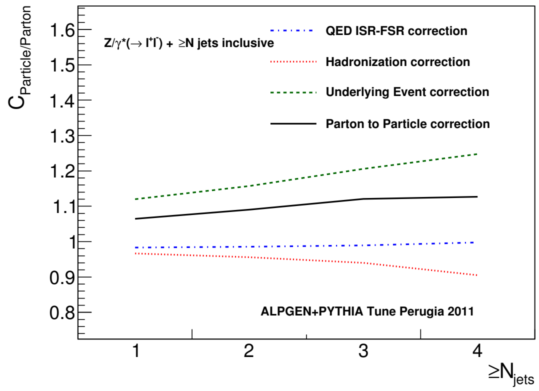

FIG. 4. Parton to particle corrections as a function of jet multiplicity. The relative contribution of QED radiation, hadronization and underlying event is shown.

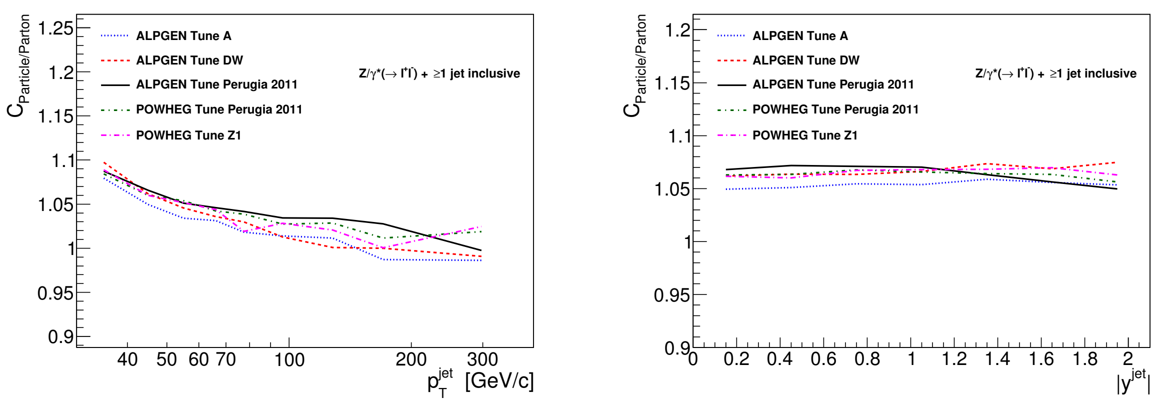

(a) (b)

FIG. 5. Parton to particle corrections as a function of (a) inclusive jet p_{T} and (b) inclusive jet rapidity for $Z/\gamma^{*} + \geqslant 1$ jet events, with different choices of the PYTHIA tune and different matrix element generators ALPGEN or POWHEG

associated to multi-parton interactions, beam remnants and hadronization. Another important effect which is not accounted for in the perturbative QCD predictions and which needs to be evaluated is the QED photon radiation from leptons and quarks. Both ISR and FSR are considered, with the main effect coming from FSR. The inclusion of QED radiation also corrects the Z/γ^{*} + jets cross sections for the contribution of $Z/\gamma^{*} + \gamma$ production, which enters the definition of the Z/γ^{*} + jets particle level used in this measurement. The non-perturbative QCD effects and the

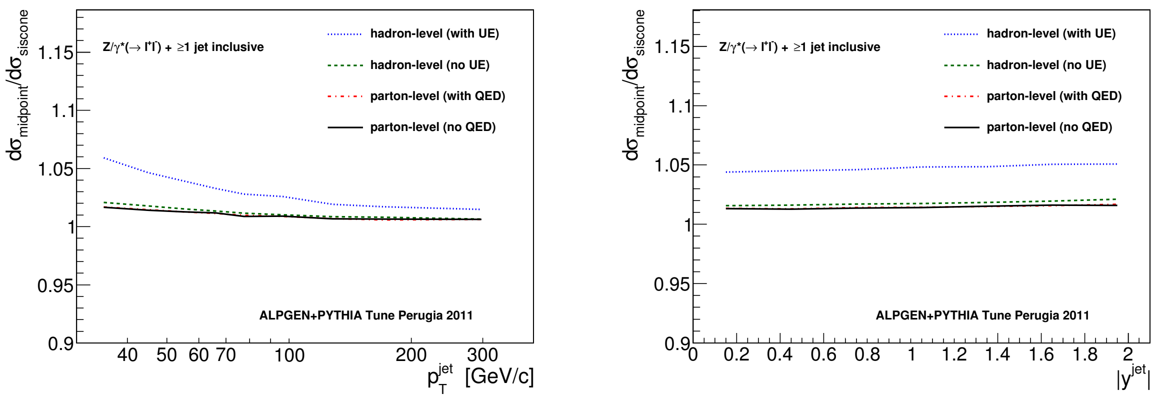

(a) (b)

FIG. 6. Comparison of CDF midpoint with the SISCone jet algorithm as a function of (a) inclusive jet $p_{\rm T}$ and (b) inclusive jet rapidity in Z/γ^{*} + $\geqslant 1$ jet events.

QED radiation are estimated with the ALPGEN+PYTHIA α_s-matched Tune Perugia 2011 Monte Carlo simulation, where the PYTHIA Monte Carlo handles the simulation of these effects. To evaluate the corrections, parton level and particle level ALPGEN+PYTHIA cross sections are defined: parton level cross sections are calculated with QED radiation, hadronization and multi-parton interactions switched off in the PYTHIA settings, while for the particle level cross sections the three switches are turned on. Kinematic requirements on leptons and jets and jet clustering parameters for the parton and particle levels are the same as those used for the measured cross sections, and photons are recombined to leptons in $\Delta R = 0.1$ whenever radiated photons are present in the final state. The corrections are obtained by evaluating the ratio of the particle to parton cross sections bin-by-bin for the various measured variables. Figure 3 shows the parton to particle correction as a function of inclusive jet $p_{\rm T}$ and inclusive jet rapidity for $Z/\gamma^{*}+\geqslant 1$ jet events, with the different contributions from QED ISR and FSR radiation, hadronization and underlying event. The corrections have a moderate dependence with the jet multiplicity, as shown in Figure 4. Figure 5 shows the parton to particle corrections evaluated with different tunes of the underlying event and hadronization model, and with the POWHEG+PYTHIA simulation. The corrections are generally below 10%, and quite independent from the PYTHIA Monte Carlo tune and from the underlying matrix element generator ALPGEN or POWHEG.

The Z/γ^{*} + jets measured cross sections employ the midpoint algorithm for the reconstruction of the jets in the final state. The midpoint algorithm belongs to the class of iterative cone

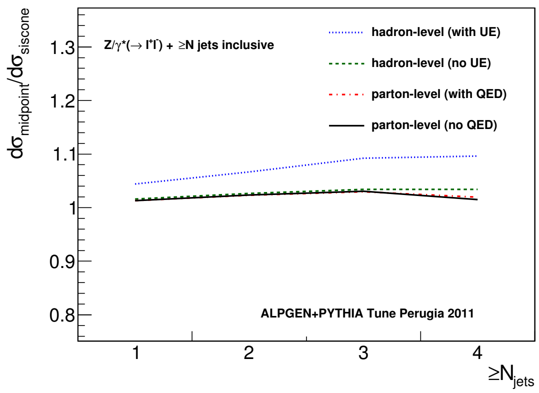

FIG. 7. Comparison of CDF midpoint with SISCone jet algorithm as a function of jet multiplicity in Z/γ^* $+ \geqslant N$ jets.

algorithms, which have been extensively used at the Tevatron. Though they present several experimental advantages, iterative cone algorithms are in general affected by infrared and collinear (IRC) safety issues. In particular the CDF midpoint jet algorithm used in this measurement is infrared unsafe, as divergences appear in a fixed order calculation for configurations with three hard particles in a common neighborhood plus a soft one, as discussed in [47, 50]. In order to compare the measured cross sections with a fixed order prediction, the strategy adopted here is to use in the prediction an infrared and collinear safe jet algorithm as close as possible to the midpoint algorithm, namely the SISCone algorithm with the same merge-split threshold $f = 0.75$ and the same jet radius $R = 0.7$ parameters of the CDF midpoint used for the measured cross sections, and to estimate the additional uncertainty coming from the use of different jet algorithms between data and theory. Figure 6 shows the cross section ratios of midpoint and SISCone jet algorithms for inclusive jet p_{T} and rapidity in $Z/\gamma^* + \geqslant 1$ jet final state. The difference at parton level between SISCone and CDF midpoint is between 2 and 3%. Higher differences between midpoint and SISCone are observed once the underlying event is switched on, however they do not affect the comparison with fixed order predictions. Figure 7 shows the same comparison as a function of jet rapidity and jet multiplicity. The difference at parton level between midpoint and SISCone is always below 3% and generally flat.

IX. RESULTS

Z/γ^* + jets differential cross sections are measured independently in the $Z/\gamma^*(\rightarrow e^+e^-)$ and $Z/\gamma^*(\rightarrow \mu^+\mu^-)$ decay channels and combined using the BLUE (Best Linear Unbiased Estimate) method [51]. The BLUE algorithm returns a weighted average of the measurements taking into account different types of uncertainty and their correlations. Systematic uncertainties related to online event selection efficiencies, lepton reconstruction efficiencies, and QCD and W + jets background estimation are considered uncorrelated between the two channels, and the other systematic uncertainties are treated as fully correlated.

Measured cross sections are compared with the LO-ME+PS Monte Carlo generator ALPGEN+PYTHIA, NLO perturbative QCD predictions from MCFM and BLACKHAT+SHERPA, NLO+PS generator POWHEG+PYTHIA, and n̄NLO LOOPSIM+MCFM predictions. MCFM predictions are available for $Z/\gamma^* + \geqslant 1$ and 2 jets final states, LOOPSIM+MCFM only for the $Z/\gamma^* + \geqslant 1$ jet final state, NLO BLACKHAT+SHERPA for jet multiplicity up to $Z/\gamma^* + \geqslant 3$ jets, and POWHEG+PYTHIA predictions are available for all the jet multiplicities but have NLO accuracy only for $Z/\gamma^* + \geqslant 1$ jet. The ALPGEN LO calculation is available for jet multiplicities up to Z/γ^* + 6 jets but for the current comparison, the calculation has been performed up to $Z/\gamma^* + \geqslant 4$ jets. NLO electro-weak corrections are available for the $Z/\gamma^* + \geqslant 1$ jet final state.

A. $Z/\gamma^* + \geqslant N$ jets cross section

The $Z/\gamma^* + \geqslant N$ jets production cross sections are measured up to $Z/\gamma^* + \geqslant 4$ jets and compared to LO and NLO perturbative QCD BLACKHAT+SHERPA, LO-ME+PS ALPGEN+PYTHIA, and NLO+PS POWHEG+PYTHIA predictions. The $Z/\gamma^* + \geqslant 1$ jet cross section is compared also to the n̄NLO LOOPSIM+MCFM prediction. Figure 8 shows the inclusive cross section as a function of jet multiplicity for $Z/\gamma^* + \geqslant 1$, 2, 3 and 4 jets, and the measured cross section is in general good agreement with all the predictions. The blue dashed bands show the theoretical uncertainty associated to the variation of the renormalization and factorization scale, except for the ALPGEN+PYTHIA prediction where the band shows the uncertainty associated to the variation of the CKKW renormalization scale. The ALPGEN+PYTHIA LO-ME+PS prediction provides a good model of the measured cross sections, but has large theoretical uncertainty at higher jet multiplicities. The BLACKHAT+SHERPA NLO perturbative QCD prediction shows a reduced scale

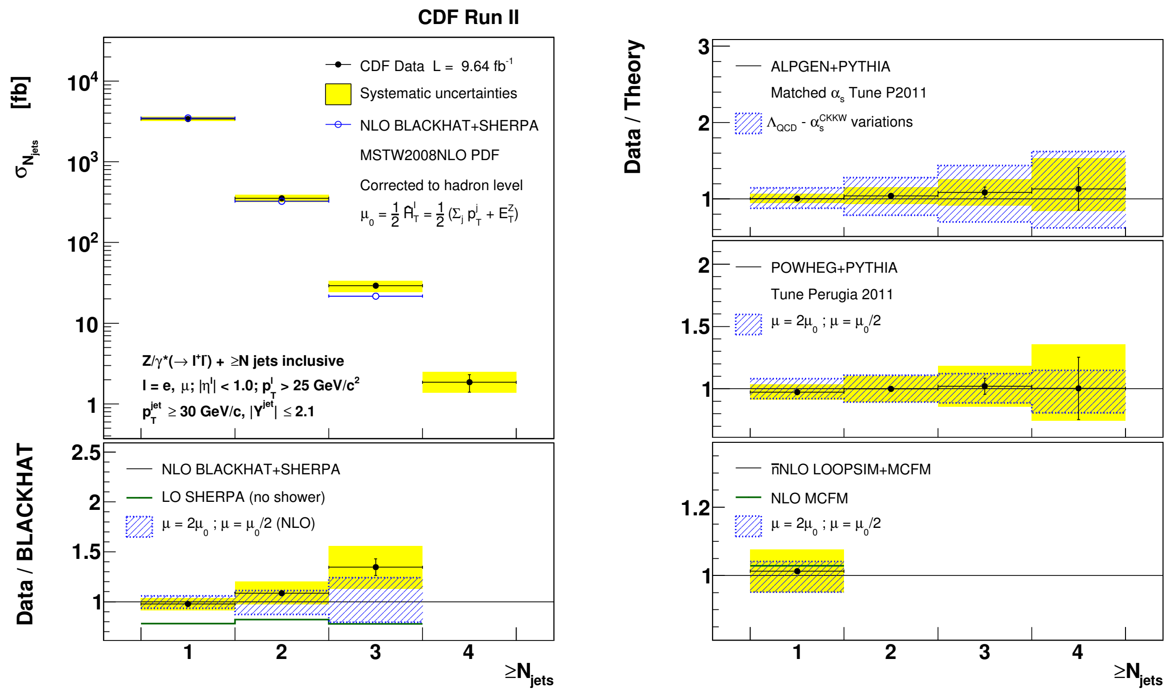

FIG. 8. $Z/\gamma^* + \geqslant N$ jets inclusive cross section as a function of jet multiplicity. The measured cross section (black dots) is compared to the BLACKHAT+SHERPA NLO prediction (open circles). The black vertical bars show the statistical uncertainty, and the yellow bands show the total systematic uncertainty, except for the 5.8% uncertainty on the luminosity. The lower and right panels show the data/theory ratio with respect to other theoretical predictions, with the blue dashed bands showing the scale uncertainty of each prediction, which is associated to the variation of the renormalization and factorization scale μ or to the combined variation of α_s^{CKKW} and Λ_{QCD}.

dependence with respect to the ALPGEN+PYTHIA LO-ME+PS prediction. The POWHEG+PYTHIA NLO+PS prediction has NLO accuracy only for $Z/\gamma^* + \geqslant 1$ jet, however it can be compared to data in all the measured jet multiplicities, where it shows a general good agreement. The LOOP-SIM+MCFM n̄NLO prediction is currently available only for $Z/\gamma^* + \geqslant 1$ jet, where it shows a very good agreement with the measured cross section and a reduced scale uncertainty at the level of 5%.

The $Z/\gamma^* + \geqslant 3$ jets BLACKHAT+SHERPA NLO perturbative QCD calculation appears to be ~30% lower than data, with the difference covered by the scale variation uncertainty. Such difference is not observed in the comparison with LO-ME+PS ALPGEN+PYTHIA and NLO+PS

POWHEG+PYTHIA predictions, and also recent measurements of Z/γ^* + jets with the ATLAS detector using the anti-kt jet algorithm [4] do not show any difference with the NLO predictions at high jet multiplicities. The reason of this difference has been thoroughly investigated in [44], and found to be related to the different angular reach [50] between the SISCone and anti-kt algorithms, and how it is influenced by additional radiation between two hard particles. The difference between data and LO-ME+PS with respect to the NLO prediction in $Z/\gamma^* + \geqslant 3$ jets final state can be explained with the presence of higher order QCD radiation, which reduces the angular reach of the SISCone algorithm and increases the cross section in this particular configuration.

B. $Z/\gamma^* + \geqslant 1$ jet differential cross sections

Figures 9 and 10 show the leading jet and inclusive jet p_{T} differential cross sections for $Z/\gamma^* + \geqslant 1$ jet events. All the theoretical predictions are in reasonable agreement with the measured cross sections. The NLO electro-weak corrections give a 5% negative contribution in the last Z/γ^* p_{T} and leading jet p_{T} bin, due to the large Sudakov logarithms which appears in the virtual part of the calculation. The scale uncertainty is quite independent of the jet p_{T} and of the order of $4-6\%$ for the $\bar{n}$NLO LOOPSIM prediction. Figure 11 shows variations in the MCFM prediction with different values of $\alpha_s(M_Z)$, factorization scale, PDF sets, and choice of the functional form of the factorization and renormalization scale.

Figure 12 shows the inclusive jet rapidity differential cross section for $Z/\gamma^* + \geqslant 1$ jet events. All the predictions correctly model this variable. In the high rapidity region the measured cross section is higher than predictions, however the difference is covered by the experimental systematic uncertainty, dominated in this region by the multiple $p\bar{p}$ interaction uncertainty. The $\bar{n}$NLO LOOPSIM+MCFM prediction has the lowest scale variation theoretical uncertainty, which is of the order of $4-6\%$, and the PDF uncertainty is between 2% and 4%. In the high rapidity region the ALPGEN prediction is lower than other theoretical models, however the difference with data is covered by the large CKKW renormalization scale uncertainty of this prediction. Figure 13 shows variations in the MCFM prediction with different values of $\alpha_s(M_Z)$, factorization scale, PDF sets, and choice of the functional form of the factorization and renormalization scale.

Figure 14 shows the Z/γ^* p_{T} differential cross section for the $Z/\gamma^* + \geqslant 1$ jet final state. The perturbative QCD fixed order calculations MCFM and LOOPSIM+MCFM fail in describing the region below the 30 GeV/c jet p_{T} threshold, where multiple jet emissions and non-perturbative QCD

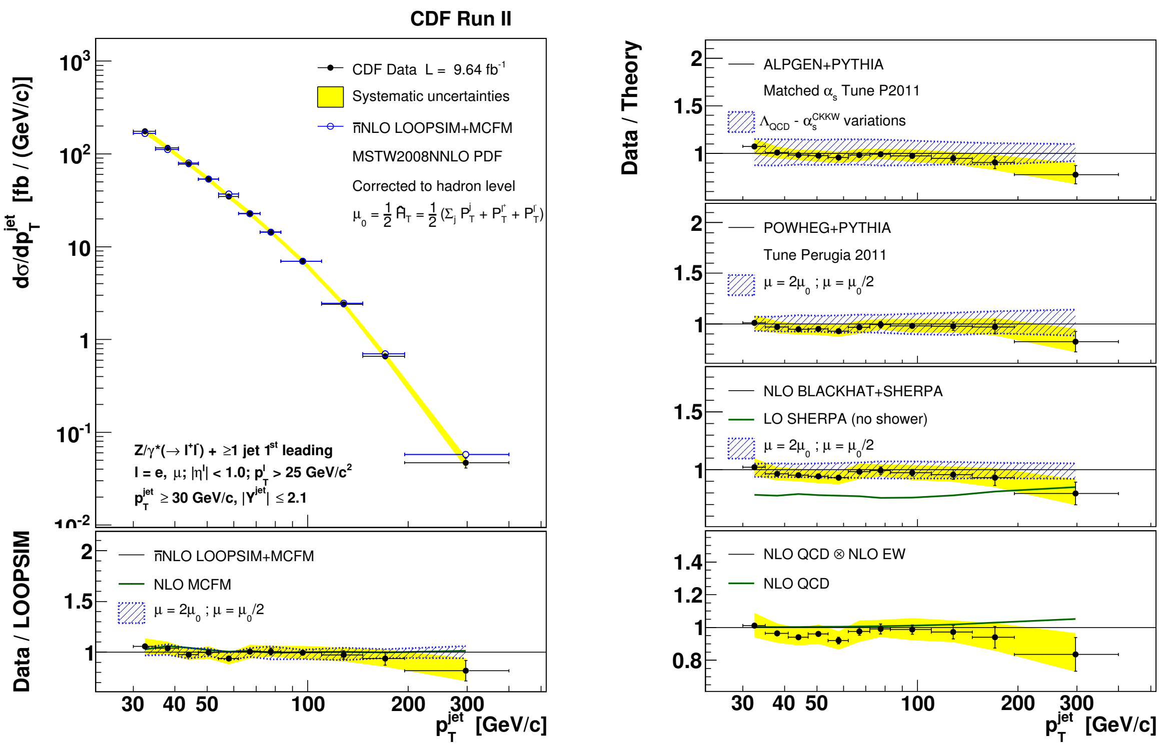

FIG. 9. Leading jet p_{T} differential cross section for $Z/\gamma^{*} + \geqslant 1$ jet events. The measured cross section (black dots) is compared to the LOOPSIM+MCFM n̄NLO prediction (open circles). The black vertical bars show the statistical uncertainty, and the yellow bands show the total systematic uncertainty, except for the 5.8% uncertainty on the luminosity. The lower and right panels show the data/theory ratio with respect to other theoretical predictions, with the blue dashed bands showing the scale uncertainty of each prediction, which is associated to the variation of the renormalization and factorization scale μ or to the combined variation of α_s^{CKKW} and Λ_{QCD}.

corrections are significant. The low Z/γ^{*} p_{T} region is better described by the ALPGEN+PYTHIA and POWHEG+PYTHIA predictions which include parton shower radiation, and in which the non-perturbative QCD corrections are applied as part of the PYTHIA Monte Carlo event evolution. In the intermediate Z/γ^{*} p_{T} region, the ratios of the data over the NLO MCFM, NLO+PS POWHEG+PYTHIA and n̄NLO LOOPSIM+MCFM predictions show a slightly concave shape which is however covered by the scale variation uncertainty. In the high Z/γ^{*} p_{T} tail the measured cross section is lower than theoretical predictions, however the difference is not statistically significant. The NLO electro-weak corrections related to the large Sudakov logarithms are negative and of the

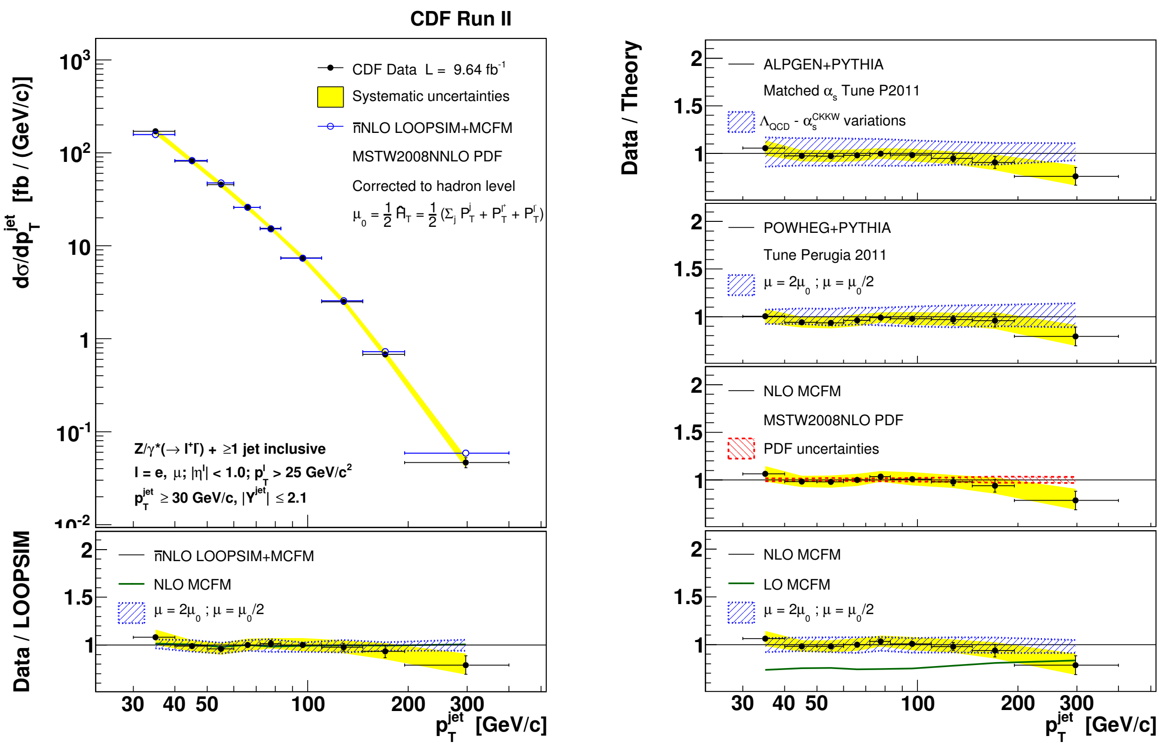

FIG. 10. Inclusive jet p_{T} differential cross section for $Z/\gamma^{*}+\geqslant 1$ jet events. The measured cross section (black dots) is compared to the LOOPSIM+MCFM $\bar{n}$NLO prediction (open circles). The black vertical bars show the statistical uncertainty, and the yellow bands show the total systematic uncertainty, except for the 5.8% uncertainty on the luminosity. The lower and right panels show the data/theory ratio with respect to other theoretical predictions, the red dashed band shows the PDF uncertainty evaluated with the MCFM prediction.

order of 5% in the last p_{T} bin.

Figure 15 shows the differential cross section as a function of Z/γ^{*}-leading jet $\Delta\phi$ variable in $Z/\gamma^{*}+\geqslant 1$ jet events. ALPGEN+PYTHIA shows a good agreement with the measured cross section in the region above $\Delta\phi = \pi/2$. In the region below $\Delta\phi = \pi/2$ the ALPGEN+PYTHIA prediction is lower than the data, with the difference covered by the scale variation uncertainty. POWHEG+PYTHIA has a very good agreement over all of the Z/γ^{*}-jet $\Delta\phi$ spectrum, and is affected by a smaller scale variation uncertainty. The difference between the ALPGEN+PYTHIA and POWHEG+PYTHIA predictions is of the same order of the experimental systematic uncertainty, in which the main contribution comes from the multiple $p\bar{p}$ interaction uncertainty, and for this rea-

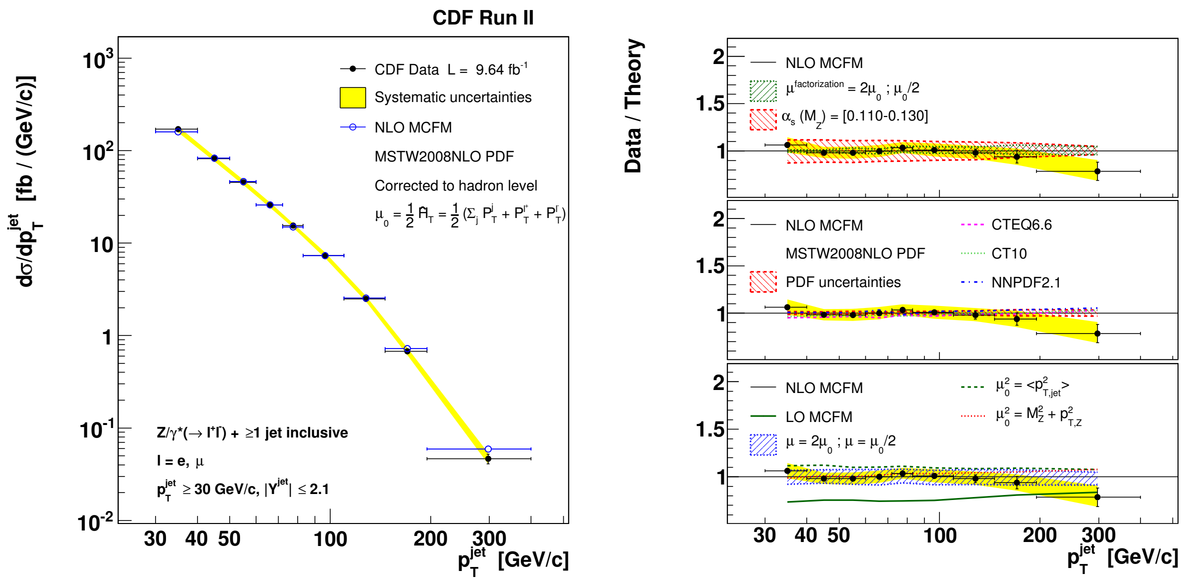

FIG. 11. Inclusive jet $p_{\rm T}$ differential cross section for $Z/\gamma^* + \geqslant 1$ jet events. The measured cross section (black dots) is compared to the MCFM NLO prediction (open circles). The black vertical bars show the statistical uncertainty, and the yellow bands show the total systematic uncertainty, except for the 5.8% uncertainty on the luminosity. The right panels show the data/theory ratio including variations of $\alpha_s(M_Z)$ and factorization scale, different PDF sets, and different choice of the functional form of the factorization and renormalization scale.

son, the measured cross section cannot be used to distinguish between the two models. The NLO MCFM prediction fails to describe the region below $\Delta\phi = \pi/2$ because it does not include the Z/γ^* + 3 jets configuration, whereas n̄NLO LOOPSIM+MCFM, which includes the Z/γ^* + 3 jets with only LO accuracy, is ∼2-3 times lower than the data in this region.

Some Z/γ^* + jets observables have larger NLO-LO K-factors and are expected to have significant beyond NLO corrections. The most remarkable example is the $H_{\rm T}^{\rm jet}$, defined as $H_{\rm T}^{\rm jet} = \sum p_{\rm T}^{\rm jet}$, in $Z/\gamma^* + \geqslant 1$ jet events. Figure 16 shows the measured cross section as a function of $H_{\rm T}^{\rm jet}$ compared to the available theoretical predictions. The NLO MCFM prediction fails to describe the shape of the $H_{\rm T}^{\rm jet}$ distribution, in particular it underestimates the measured cross section in the high $H_{\rm T}^{\rm jet}$ region where the NLO-LO K-factor $\gtrsim 2$ and a larger NLO scale variation uncertainty is observed. The LO-ME+PS ALPGEN+PYTHIA prediction is in good agreement with data, but suffers for the large LO scale uncertainty. Also the POWHEG+PYTHIA is in good agreement with data, but is

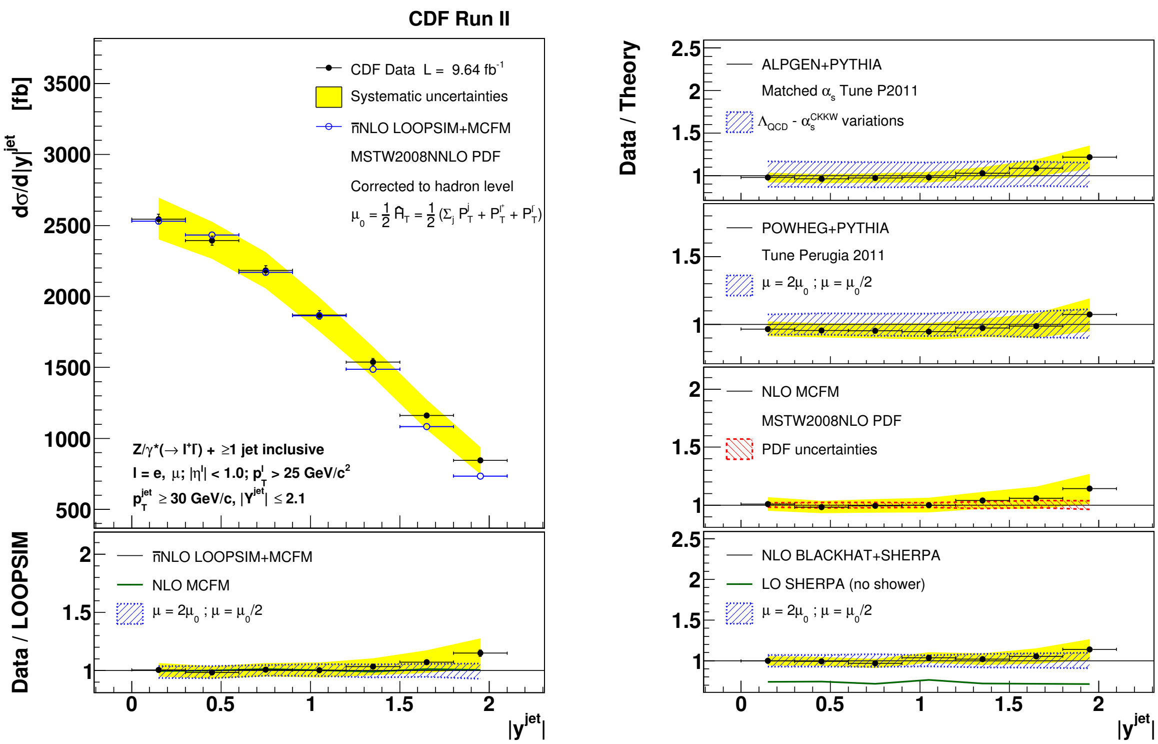

FIG. 12. $Z/\gamma^*+\geqslant 1$ jet differential cross section as a function of inclusive jet rapidity. The measured cross section (black dots) is compared to the LOOPSIM+MCFM n̄NLO prediction (open circles). The black vertical bars show the statistical uncertainty, and the yellow bands show the total systematic uncertainty, except for the 5.8% uncertainty on the luminosity. The lower and right panels show the data/theory ratio with respect to other theoretical predictions, with the blue dashed bands showing the scale uncertainty of each prediction, which is associated to the variation of the renormalization and factorization scale μ or to the combined variation of α_s^{CKKW} and Λ_{QCD}.

still affected by the larger NLO scale uncertainty in the high p_T tail. The n̄NLO LOOPSIM+MCFM prediction provides a good modelling of the data distribution, and shows a significantly reduced scale uncertainty.

C. $Z/\gamma^*+\geqslant 2$ jets differential cross sections

Figures 17 to 23 show measured differential cross sections in the $Z/\gamma^*+\geqslant 2$ jets final state. Figures 17 and 18 show the measured cross section as a function of the 2$^{\text{nd}}$ leading jet p_T and

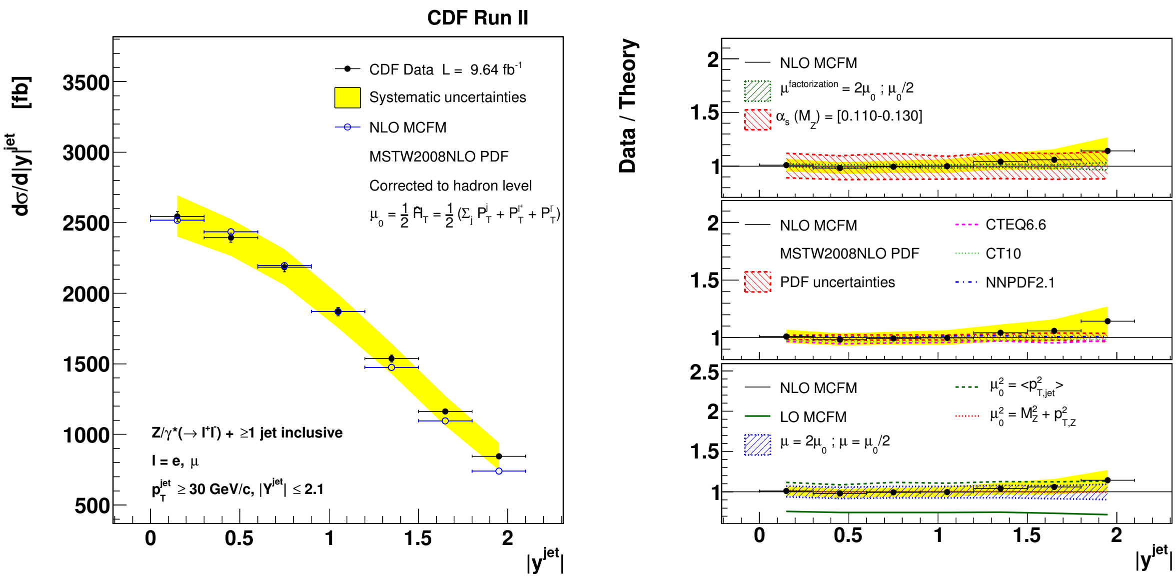

FIG. 13. $Z/\gamma^{*}+\geqslant 1$ jet differential cross section as a function of inclusive jet rapidity. The measured cross section (black dots) is compared to the MCFM NLO prediction (open circles). The black vertical bars show the statistical uncertainty, and the yellow bands show the total systematic uncertainty, except for the 5.8% uncertainty on the luminosity. The right panels show the data/theory ratio including variations of $\alpha_s(M_Z)$ and factorization scale, different PDF sets, and different choice of the functional form of the factorization and renormalization scale.

inclusive jet rapidity compared to ALPGEN+PYTHIA and BLACKHAT+SHERPA predictions. Measured distributions are in good agreement with the theoretical predictions. Figure 19 shows the measured cross section as a function of the di-jet mass M_{jj}. The first bin at M_{jj} $40-60$ GeV/c^2 is overestimated by the MCFM prediction, but correctly described by the ALPGEN+PYTHIA prediction. In the high M_{jj} region above $\sim$160 GeV/c^2, the measured cross sections are $10-20\%$ higher than both predictions. However the systematic uncertainty, mainly due to the jet energy scale, is as large as the observed difference. Figure 20 shows the measured cross section as a function of the di-jet ΔR compared to ALPGEN+PYTHIA and MCFM predictions. Some difference between data and theory is observed at high ΔR, where the measured cross section is $\sim$50% higher than the theoretical predictions. Also the di-jet $\Delta\phi$ and Δy differential cross sections have been measured, and the results are shown in Figures 21 and 22. The di-jet $\Delta\phi$ appears reasonably modeled by the ALPGEN+PYTHIA and MCFM predictions, while the di-jet Δy shows a shape difference which

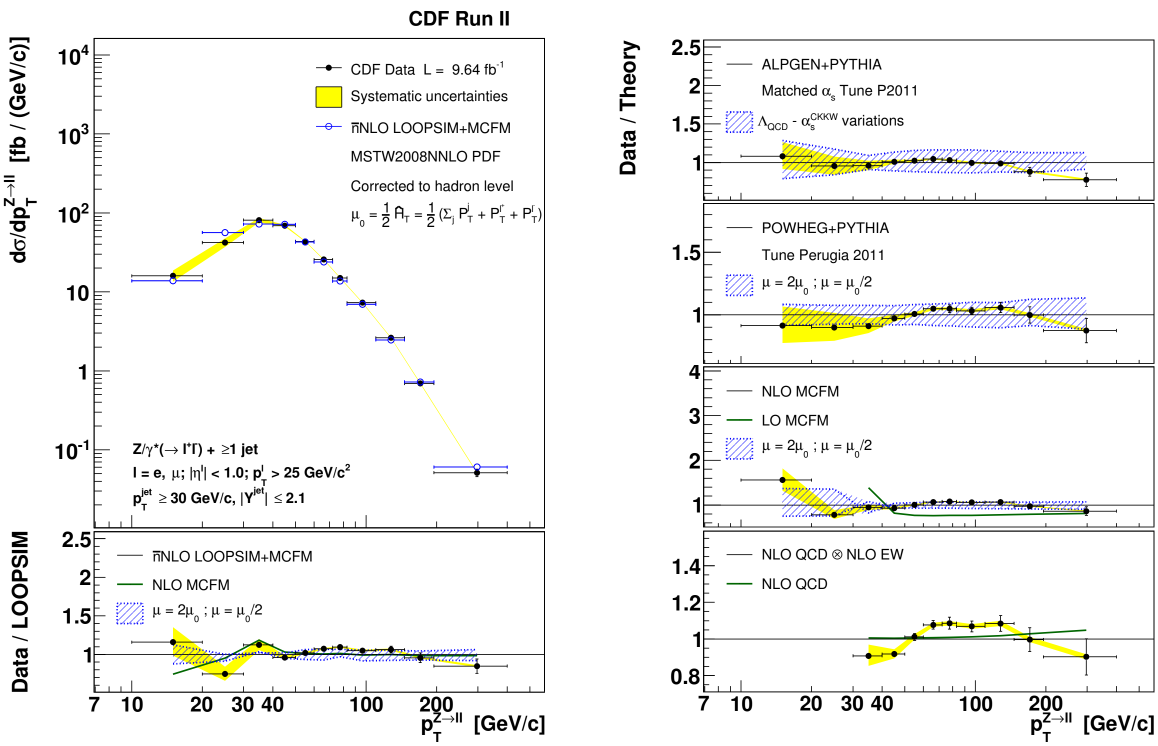

FIG. 14. $Z/\gamma^{*}+\geqslant 1$ jet differential cross section as a function of Z/γ^{*} p_{T}. The measured cross section (black dots) is compared to the LOOPSIM+MCFM n̄NLO prediction (open circles). The black vertical bars show the statistical uncertainty, and the yellow bands show the total systematic uncertainty, except for the 5.8% uncertainty on the luminosity. The lower and right panels show the data/theory ratio with respect to other theoretical predictions, with the blue dashed bands showing the scale uncertainty of each prediction, which is associated to the variation of the renormalization and factorization scale μ or to the combined variation of α_s^{CKKW} and Λ_{QCD}.

is as large as 50% at $\Delta y = 3-3.6$, and is related to the observed difference between data and theory at $\Delta R \gtrsim 4$. This region is affected by large experimental uncertainty, mainly due to the pile-up subtraction, and large theoretical uncertainty. Figure 23 shows the measured cross section as a function of the dihedral angle $\theta_{Z,jj}$ between the $Z/\gamma^{*}(\rightarrow l^{+}l^{-})$ decay plane and the jet-jet plane [52].

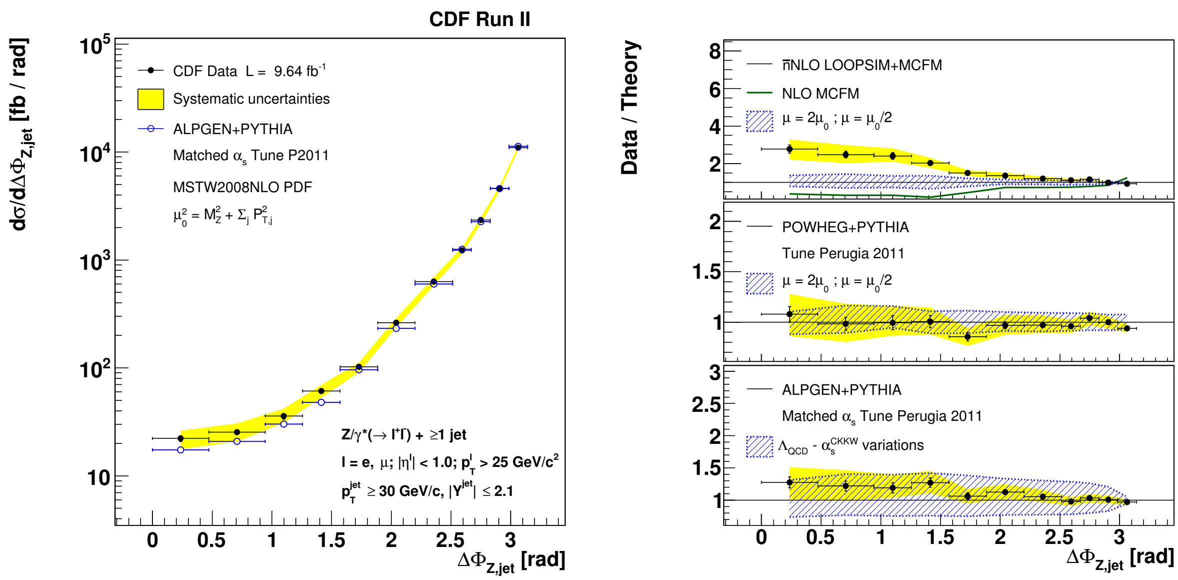

FIG. 15. $Z/\gamma^{*}+\geqslant 1$ jet differential cross section as a function of Z/γ^{*}-jet $\Delta\phi$. The measured cross section (black dots) is compared to the LOOPSIM+MCFM n̄NLO prediction (open circles). The black vertical bars show the statistical uncertainty, and the yellow bands show the total systematic uncertainty, except for the 5.8% uncertainty on the luminosity. The right panels show the data/theory ratio with respect to other theoretical predictions, with the blue dashed bands showing the scale uncertainty of each prediction, which is associated to the variation of the renormalization and factorization scale μ or to the combined variation of α_s^{CKKW} and Λ_{QCD}.

D. $Z/\gamma^{*}+\geqslant 3$ jets differential cross sections

Figure 24 shows the differential cross sections as a functions of 3$^{\rm rd}$ leading jet $p_{\rm T}$ and inclusive jet rapidity in events with a reconstructed $Z/\gamma^{*}(\rightarrow l^{+}l^{-})$ and at least 3 jets. As already discussed, the NLO BLACKHAT+SHERPA prediction is ∼30% lower than the measured cross sections for $Z/\gamma^{*}+\geqslant 3$ jets events, however data and predictions are still compatible within the large scale variation uncertainty which is of the order of 25%, and the experimental systematic uncertainty which is ∼15% and dominated by the jet energy scale. Apart from the difference in the normalization, the shape of the measured differential cross sections is in good agreement with the NLO BLACKHAT+SHERPA prediction.

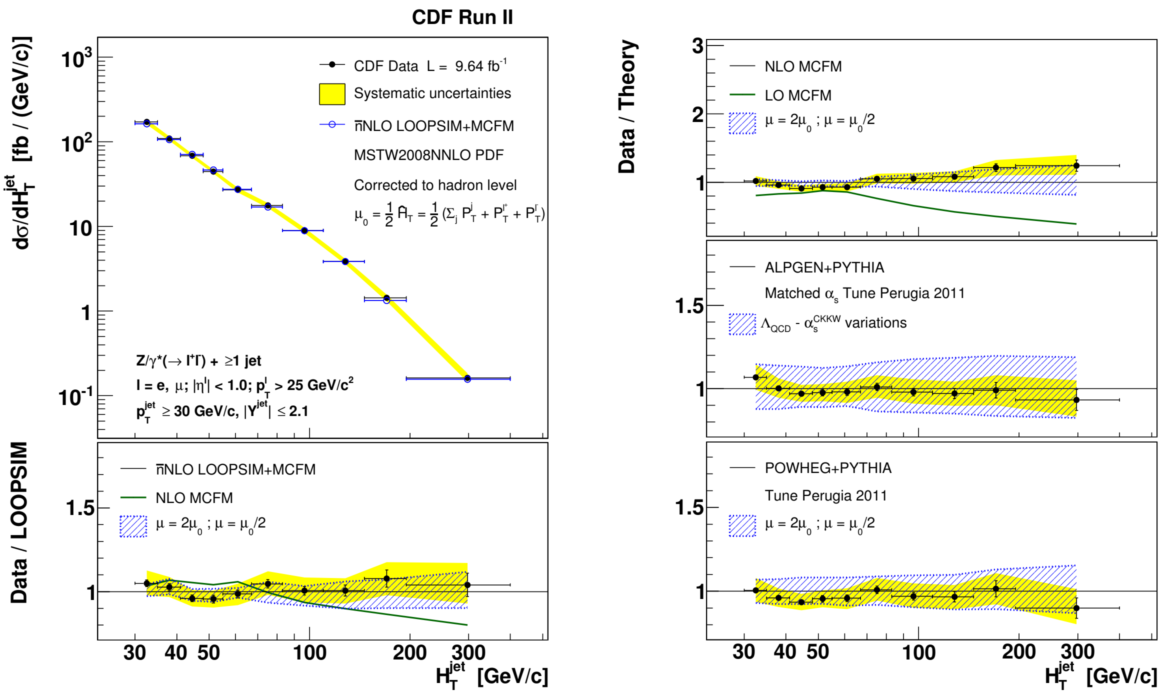

FIG. 16. $Z/\gamma^* + \geqslant 1$ jet differential cross section as a function of $H_T^{\text{jet}} = \sum p_T^{\text{jet}}$. The measured cross section (black dots) is compared to the LOOPSIM+MCFM n̄NLO prediction (open circles). The black vertical bars show the statistical uncertainty, and the yellow bands show the total systematic uncertainty, except for the 5.8% uncertainty on the luminosity. The lower and right panels show the data/theory ratio with respect to other theoretical predictions, with the blue dashed bands showing the scale uncertainty of each prediction, which is associated to the variation of the renormalization and factorization scale μ or to the combined variation of α_s^{CKKW} and Λ_{QCD}.

X. SUMMARY AND CONCLUSIONS

The analysis of 9.6 fb^{-1} of integrated luminosity, corresponding to the full dataset collected with the CDF detector in Run II, allows for precise measurement of Z/γ^* + jets inclusive and differential cross sections, which constitutes an important legacy of the Tevatron physics program. The understanding of vector boson + jets processes is fundamental in the search for new physics, and the results presented in this paper validate the modelling of Z/γ^* + jets currently employed in Higgs and beyond the standard model searches. The cross sections of the $Z/\gamma^*(\to e^+e^-)$ and $Z/\gamma^*(\to \mu^+\mu^-)$ decay channels are measured in the kinematic region $p_T^l \geqslant 25$ GeV/c, $|\eta^l| \leqslant 1$,

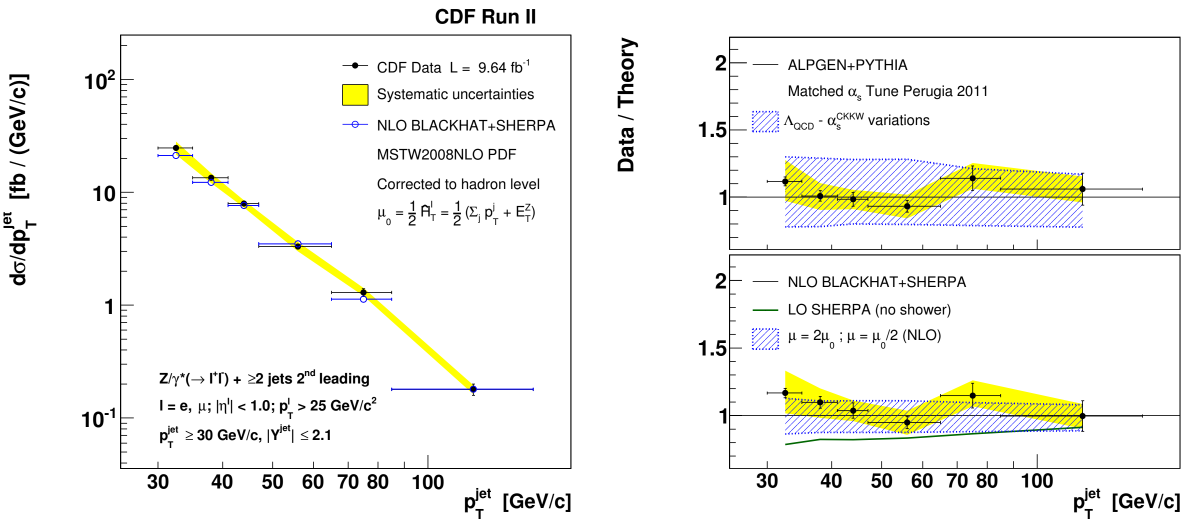

FIG. 17. $Z/\gamma^{*}+\geqslant 2$ jets differential cross section as a function of 2nd leading jet p_{T}. The measured cross section (black dots) is compared to the BLACKHAT+SHERPA NLO prediction (open circles). The black vertical bars show the statistical uncertainty, and the yellow bands show the total systematic uncertainty, except for the 5.8% uncertainty on the luminosity. The right panels show the data/theory ratio with respect to ALPGEN+PYTHIA and BLACKHAT+SHERPA predictions, with the blue dashed bands showing the scale uncertainty of each prediction, which is associated to the variation of the renormalization and factorization scale μ or to the combined variation of α_s^{CKKW} and Λ_{QCD}.

$66 \leqslant M_{l^+l^-} \leqslant 116$ GeV$/c^2$, $p_{\mathrm{T}}^{\mathrm{jet}} \geqslant 30$ GeV/c, $|y^{\mathrm{jet}}| \leqslant 2.1|$ and $\Delta R_{\mathrm{lepton-jet}} > 0.7$ with jets reconstructed using the midpoint algorithm in a radius $R = 0.7$. These cross sections are unfolded to the particle level and combined. Results are compared with the most recent theoretical predictions, which properly model the measured differential cross sections in $Z/\gamma^{*}+\geqslant 1$, 2 and 3 jets final states. The main experimental uncertainty is related to the jet energy scale, while the largest uncertainty of the theoretical predictions is generally associated to the variation of the renormalization and factorization scale. Among perturbative QCD predictions, LOOPSIM+MCFM shows the lowest scale variation uncertainty and is the most accurate prediction for the $Z/\gamma^{*}+\geqslant 1$ jet final state. NLO fixed order predictions MCFM and BLACKHAT+SHERPA are in reasonable agreement with the data in the $Z/\gamma^{*}+\geqslant 1,2,3$ jets final states. The ALPGEN+PYTHIA prediction provides a good modelling of differential distributions in all the jets multiplicity. The POWHEG+PYTHIA prediction, due to the NLO accuracy of the matrix elements and to the inclusion of non-perturbative

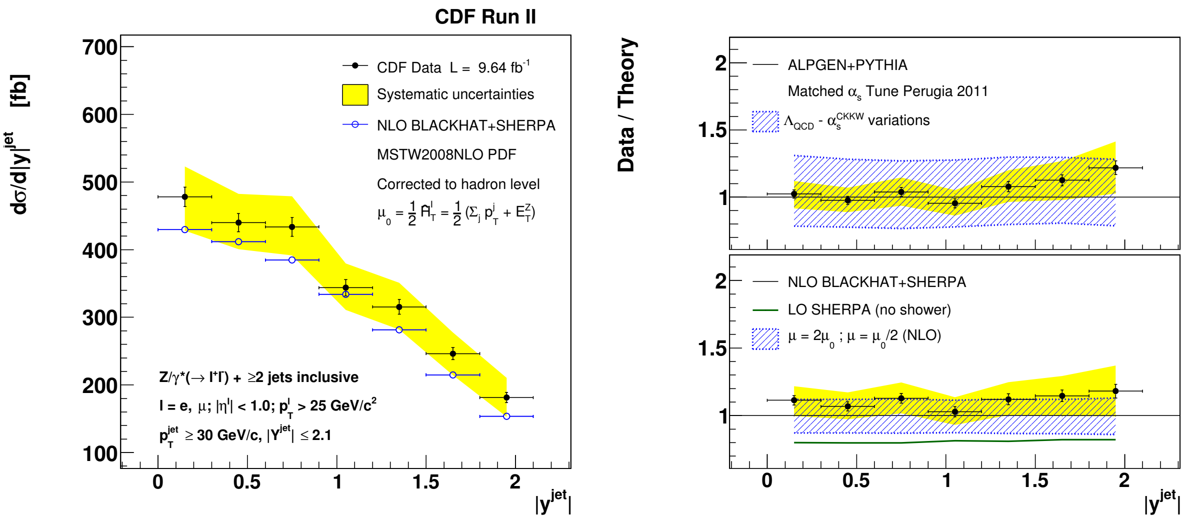

FIG. 18. $Z/\gamma^{*}+\geqslant 2$ jets differential cross section as a function of inclusive jet rapidity. The measured cross section (black dots) is compared to the BLACKHAT+SHERPA NLO prediction (open circles). The black vertical bars show the statistical uncertainty, and the yellow bands show the total systematic uncertainty, except for the 5.8% uncertainty on the luminosity. The right panels show the data/theory ratio with respect to ALPGEN+PYTHIA and BLACKHAT+SHERPA predictions, with the blue dashed bands showing the scale uncertainty of each prediction, which is associated to the variation of the renormalization and factorization scale μ or to the combined variation of α_s^{CKKW} and Λ_{QCD}.

QCD effects, provides precise modelling of $Z/\gamma^{*}+\geqslant 1$ jet final state both in the low and high p_{T} kinematic regions. The effect of NLO electro-weak virtual corrections to the Z/γ^{*} + jet production has been studied and included in the comparison with the measured cross sections: in the high p_{T} kinematic region corrections are of the order of 5%, which is comparable with the accuracy of beyond NLO predictions.

ACKNOWLEDGMENTS

We thank the Fermilab staff and the technical staffs of the participating institutions for their vital contributions. This work was supported by the U.S. Department of Energy and National Science Foundation; the Italian Istituto Nazionale di Fisica Nucleare; the Ministry of Education, Culture, Sports, Science and Technology of Japan; the Natural Sciences and Engineering Research

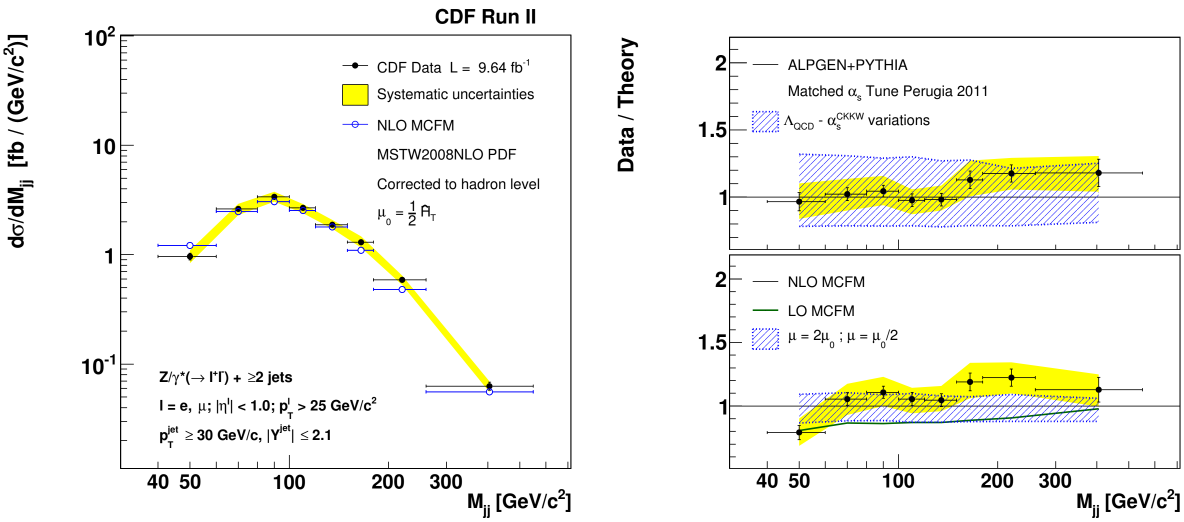

FIG. 19. $Z/\gamma^{*} + \geqslant 2$ jets differential cross section as a function of di-jet mass M_{jj}. The measured cross section (black dots) is compared to the MCFM NLO prediction (open circles). The black vertical bars show the statistical uncertainty, and the yellow bands show the total systematic uncertainty, except for the 5.8% uncertainty on the luminosity. The right panels show the data/theory ratio with respect to ALPGEN+PYTHIA and MCFM predictions, with the blue dashed bands showing the scale uncertainty of each prediction, which is associated to the variation of the renormalization and factorization scale μ or to the combined variation of α_s^{CKKW} and Λ_{QCD}.

Council of Canada; the National Science Council of the Republic of China; the Swiss National Science Foundation; the A.P. Sloan Foundation; the Bundesministerium für Bildung und Forschung, Germany; the Korean World Class University Program, the National Research Foundation of Korea; the Science and Technology Facilities Council and the Royal Society, United Kingdom; the Russian Foundation for Basic Research; the Ministerio de Ciencia e Innovación, and Programa Consolider-Ingenio 2010, Spain; the Slovak R&D Agency; the Academy of Finland; the Australian Research Council (ARC); and the EU community Marie Curie Fellowship Contract No. 302103.

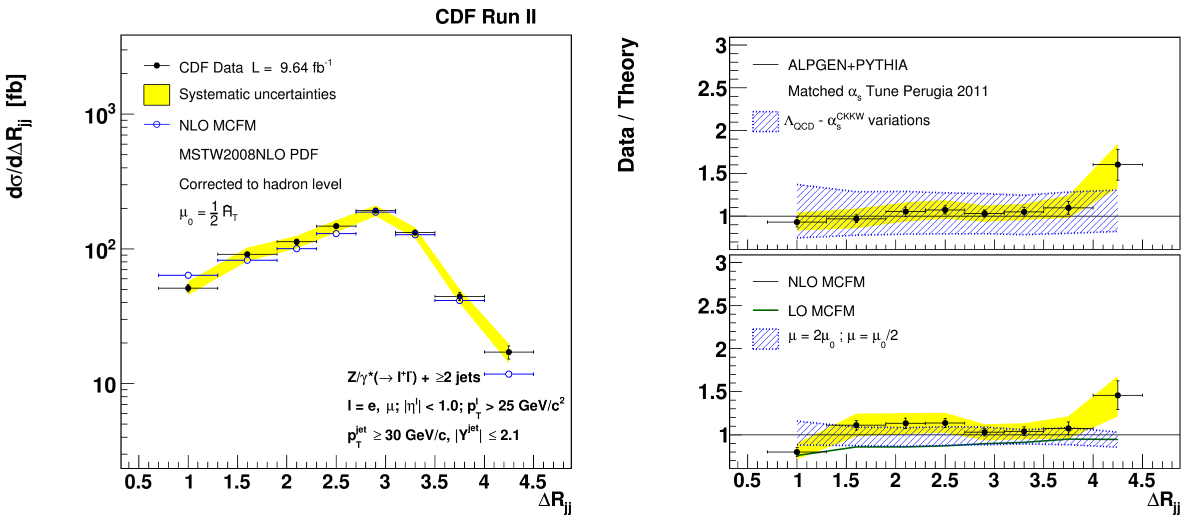

FIG. 20. $Z/\gamma^{*}+\geqslant 2$ jets differential cross section as a function of di-jet ΔR. The measured cross section (black dots) is compared to the MCFM NLO prediction (open circles). The black vertical bars show the statistical uncertainty, and the yellow bands show the total systematic uncertainty, except for the 5.8% uncertainty on the luminosity. The right panels show the data/theory ratio with respect to ALPGEN+PYTHIA and MCFM predictions, with the blue dashed bands showing the scale uncertainty of each prediction, which is associated to the variation of the renormalization and factorization scale μ or to the combined variation of α_s^{CKKW} and Λ_{QCD}.

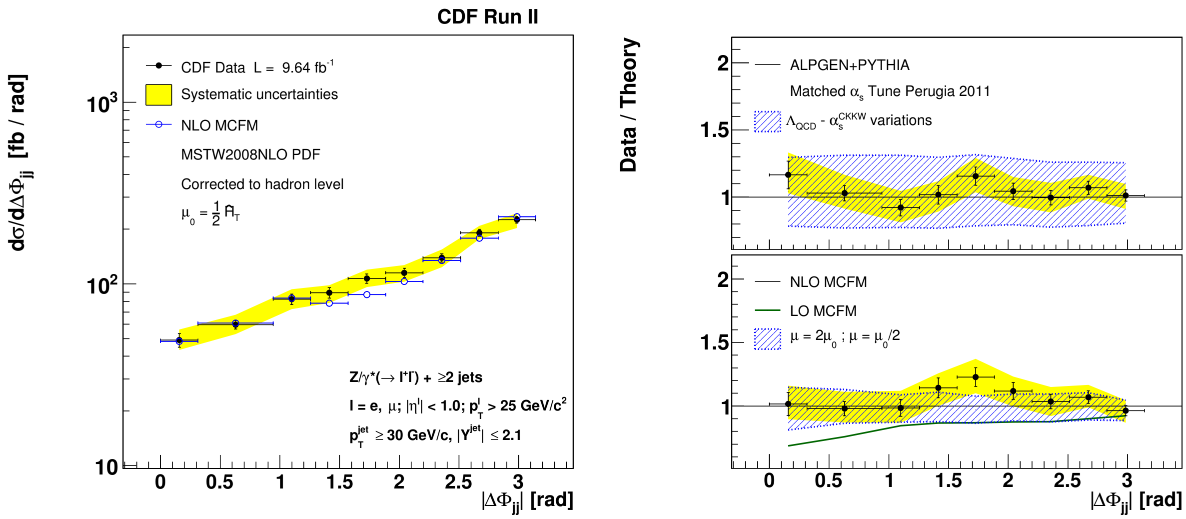

FIG. 21. $Z/\gamma^* + \geqslant 2$ jets differential cross section as a function of di-jet $\Delta\phi$. The measured cross section (black dots) is compared to the MCFM NLO prediction (open circles). The black vertical bars show the statistical uncertainty, and the yellow bands show the total systematic uncertainty, except for the 5.8% uncertainty on the luminosity. The right panels show the data/theory ratio with respect to ALPGEN+PYTHIA and MCFM predictions, with the blue dashed bands showing the scale uncertainty of each prediction, which is associated to the variation of the renormalization and factorization scale μ or to the combined variation of α_s^{CKKW} and Λ_{QCD}.

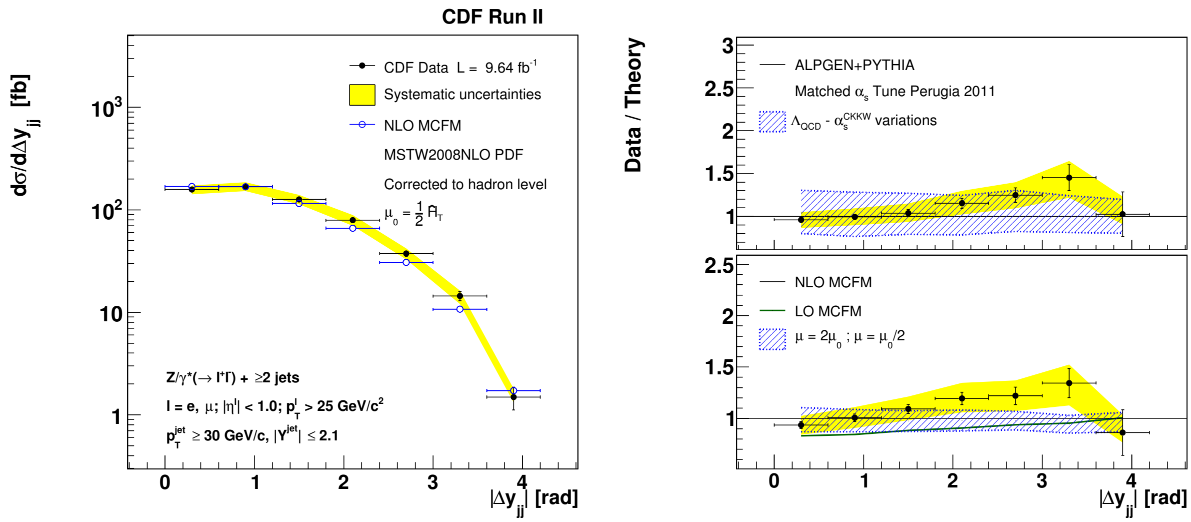

FIG. 22. $Z/\gamma^*+ \geqslant 2$ jets differential cross section as a function of di-jet Δy. The measured cross section (black dots) is compared to the MCFM NLO prediction (open circles). The black vertical bars show the statistical uncertainty, and the yellow bands show the total systematic uncertainty, except for the 5.8% uncertainty on the luminosity. The right panels show the data/theory ratio with respect to ALPGEN+PYTHIA and MCFM predictions, with the blue dashed bands showing the scale uncertainty of each prediction, which is associated to the variation of the renormalization and factorization scale μ or to the combined variation of α_s^{CKKW} and Λ_{QCD}.

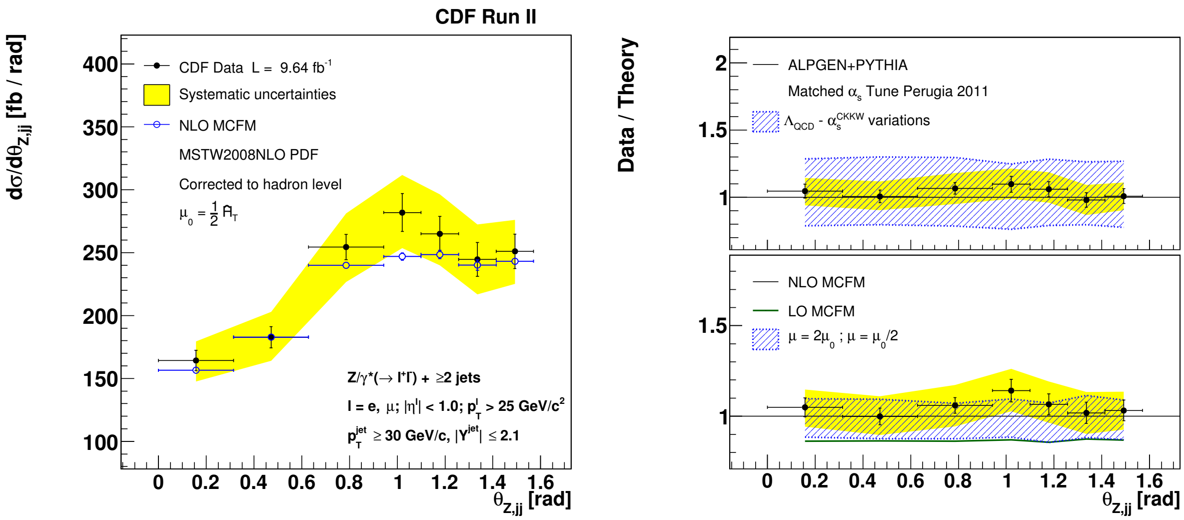

FIG. 23. $Z/\gamma^{*}+\geqslant 2$ jets differential cross section as a function of the dihedral angle $\theta_{Z,jj}$. The measured cross section (black dots) is compared to the MCFM NLO prediction (open circles). The black vertical bars show the statistical uncertainty, and the yellow bands show the total systematic uncertainty, except for the 5.8% uncertainty on the luminosity. The right panels show the data/theory ratio with respect to ALPGEN+PYTHIA and MCFM predictions, with the blue dashed bands showing the scale uncertainty of each prediction, which is associated to the variation of the renormalization and factorization scale μ or to the combined variation of α_s^{CKKW} and Λ_{QCD}.

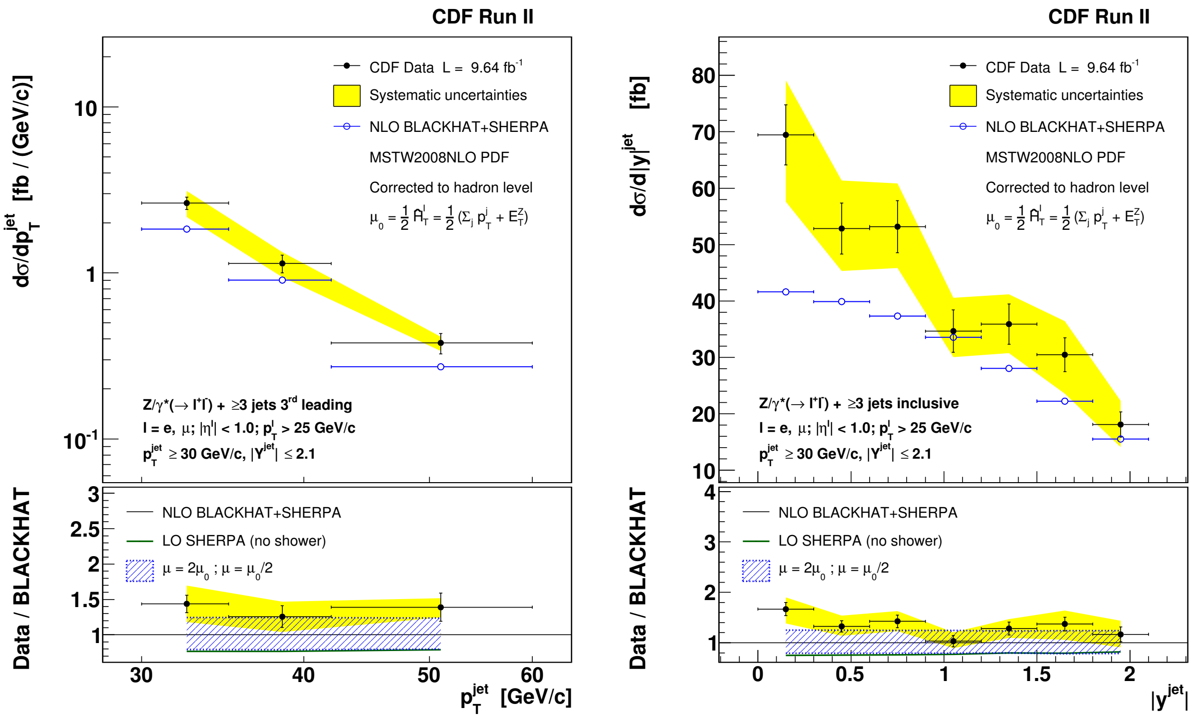

(a) (b)

FIG. 24. $Z/\gamma^{*} + \geqslant 3$ jets differential cross section as a function of (a) 3$^{\rm rd}$ leading jet $p_{\rm T}$ and (b) inclusive jet rapidity. The measured cross section (black dots) is compared to the BLACKHAT+SHERPA NLO prediction (open circles). The black vertical bars show the statistical uncertainty, and the yellow bands show the total systematic uncertainty, except for the 5.8% uncertainty on the luminosity. The lower panels show the the data/theory ratio, with the blue dashed bands showing the scale uncertainty, which is associated to the variation of the renormalization and factorization scale μ.

[1] D. Gross and F. Wilczek, Phys. Rev. D **8**, 3633 (1973).

[2] T. Aaltonen *et al.* (CDF Collaboration), Phys. Rev. Lett. **100**, 102001 (2008), arXiv:0711.3717 [hep-ex].

[3] V. Abazov *et al.* (D0 Collaboration), Phys. Lett. B **669**, 278 (2008), arXiv:0808.1296 [hep-ex]; Phys. Lett. B **678**, 45 (2009), arXiv:0903.1748 [hep-ex]; Phys. Lett. B **682**, 370 (2010), arXiv:0907.4286 [hep-ex].

[4] G. Aad *et al.* (ATLAS Collaboration), J. High Energy Phys. 1307 (2013) 032, arXiv:1304.7098 [hep-ex]; Phys. Rev. D **85**, 032009 (2012), arXiv:1111.2690 [hep-ex].

[5] S. Chatrchyan *et al.* (CMS Collaboration), J. High Energy Phys. 1201 (2012) 010, arXiv:1110.3226 [hep-ex]; Phys. Lett. B **722**, 238 (2013), arXiv:1301.1646 [hep-ex].

[6] The rapidity is defined as $y = \frac{1}{2}\ln(\frac{E+p_Z}{E-p_Z})$, the transverse momentum and energy are defined by $p_T = p\sin\theta$ and $E_T = E\sin\theta$.

[7] J. M. Campbell and R. K. Ellis, Phys. Rev. D **65**, 113007 (2002), arXiv:hep-ph/0202176 [hep-ph].

[8] C. Berger, Z. Bern, L. Dixon, F. Febres Cordero, D. Forde, *et al.*, Phys. Rev. D **78**, 036003 (2008), arXiv:0803.4180 [hep-ph].

[9] M. Rubin, G. P. Salam, and S. Sapeta, J. High Energy Phys. 1009 (2010) 084, arXiv:1006.2144 [hep-ph].

[10] A. Denner, S. Dittmaier, T. Kasprzik, and A. Muck, J. High Energy Phys. 1106 (2011) 069, arXiv:1103.0914 [hep-ph].

[11] M. L. Mangano, M. Moretti, F. Piccinini, R. Pittau, and A. D. Polosa, J. High Energy Phys. 0307 (2003) 001, arXiv:hep-ph/0206293 [hep-ph].

[12] S. Alioli, P. Nason, C. Oleari, and E. Re, J. High Energy Phys. 1101 (2011) 095, arXiv:1009.5594 [hep-ph].

[13] A. Abulencia *et al.* (CDF Collaboration), J. Phys. G **34**, 2457 (2007), arXiv:hep-ex/0508029 [hep-ex].

[14] B. Winer, Int. J. Mod. Phys. **A16S1C**, 1169 (2001).

[15] A. Abulencia *et al.* (CDF Collaboration), Phys. Rev. D **74**, 071103 (2006), arXiv:hep-ex/0512020 [hep-ex].

[16] The jet cone radius R is defined as $R = \sqrt{\eta^2 + \phi^2}$.

[17] The transverse energy is evaluated using the position of the tower with respect to the primary interaction vertex.

[18] G. C. Blazey, J. R. Dittmann, S. D. Ellis, V. D. Elvira, K. Frame, *et al.*, FERMILAB-CONF-00-092-E (2000), arXiv:hep-ex/0005012 [hep-ex].

[19] A. Bhatti *et al.* (CDF Collaboration), Nucl. Instrum. Meth. A **566**, 375 (2006), arXiv:hep-ex/0510047 [hep-ex].

[20] ΔR is defined as $\Delta R = \sqrt{\Delta y^2 + \Delta\phi^2}$.

[21] T. Sjostrand, S. Mrenna, and P. Z. Skands, J. High Energy Phys. 0605 (2006) 026, arXiv:hep-ph/0603175 [hep-ph].

[22] H. Lai *et al.* (CTEQ Collaboration), Eur. Phys. J. C **12**, 375 (2000), arXiv:hep-ph/9903282 [hep-ph].

[23] P. Z. Skands, Phys. Rev. D **82**, 074018 (2010), arXiv:1005.3457 [hep-ph].

[24] J. Alwall, S. Hoche, F. Krauss, N. Lavesson, L. Lonnblad, *et al.*, Eur. Phys. J. C **53**, 473 (2008), arXiv:0706.2569 [hep-ph].

[25] T. Affolder *et al.* (CDF Collaboration), Phys. Rev. D **65**, 092002 (2002).

[26] R. Brun, F. Bruyant, M. Maire, A. McPherson, and P. Zanarini, CERN-DD-EE-84-1 (1987).

[27] G. Grindhammer, M. Rudowicz, and S. Peters, Nucl. Instrum. Meth. A **290**, 469 (1990).

[28] S. Moch and P. Uwer, Nucl. Phys. Proc. Suppl. **183**, 75 (2008), arXiv:0807.2794 [hep-ph].

[29] J. M. Campbell and R. K. Ellis, Phys. Rev. D **60**, 113006 (1999), arXiv:hep-ph/9905386 [hep-ph].

[30] C. Buttar, J. D'Hondt, M. Kramer, G. Salam, M. Wobisch, *et al.*, (2008), arXiv:0803.0678 [hep-ph].

[31] S. Klimenko, J. Konigsberg, and T. M. Liss, FERMILAB-FN-0741 (2003).

[32] A. Martin, W. Stirling, R. Thorne, and G. Watt, Eur. Phys. J. C **63**, 189 (2009), arXiv:0901.0002 [hep-ph].

[33] J. Pumplin, D. Stump, R. Brock, D. Casey, J. Huston, *et al.*, Phys. Rev. D **65**, 014013 (2001), arXiv:hep-ph/0101032 [hep-ph].

[34] P. M. Nadolsky, H.-L. Lai, Q.-H. Cao, J. Huston, J. Pumplin, *et al.*, Phys. Rev. D **78**, 013004 (2008), arXiv:0802.0007 [hep-ph].

[35] R. D. Ball, V. Bertone, F. Cerutti, L. Del Debbio, S. Forte, *et al.*, Nucl. Phys. **B849**, 296 (2011), arXiv:1101.1300 [hep-ph].

[36] H.-L. Lai, M. Guzzi, J. Huston, Z. Li, P. M. Nadolsky, *et al.*, Phys. Rev. D **82**, 074024 (2010), arXiv:1007.2241 [hep-ph].

[37] A. D. Martin, R. Roberts, W. Stirling, and R. Thorne, Eur. Phys. J. C **23**, 73 (2002), arXiv:hep-ph/0110215 [hep-ph].

[38] M. Whalley, D. Bourilkov, and R. Group, (2005), arXiv:hep-ph/0508110 [hep-ph].

[39] In BLACKHAT and POWHEG predictions the alternative definition $\mu_0 = \hat{H}'_T/2 = \frac{1}{2}\left(\sum_j p_T^j + E_T^Z\right)$ with $E_T^Z = \sqrt{M_Z^2 + p_{T,Z}^2}$ is used.

[40] C. Berger, Z. Bern, L. J. Dixon, F. Febres Cordero, D. Forde, *et al.*, Phys. Rev. D **82**, 074002 (2010), arXiv:1004.1659 [hep-ph]; Phys. Rev. D **80**, 074036 (2009), arXiv:0907.1984 [hep-ph].

[41] C. W. Bauer and B. O. Lange, (2009), arXiv:0905.4739 [hep-ph].

[42] S. Catani, F. Krauss, R. Kuhn, and B. Webber, J. High Energy Phys. 0111 (2001) 063, arXiv:hep-ph/0109231 [hep-ph].

[43] B. Cooper, J. Katzy, M. Mangano, A. Messina, L. Mijovic, *et al.*, Eur. Phys. J. C **72**, 2078 (2012), arXiv:1109.5295 [hep-ph].

[44] S. Camarda, Ph.D. thesis, Universitat Autonoma de Barcelona, FERMILAB-THESIS-2012-12, 2012.

[45] S. D. Ellis, Z. Kunszt, and D. E. Soper, Phys. Rev. Lett. **69**, 3615 (1992), arXiv:hep-ph/9208249 [hep-ph].

[46] M. Cacciari, G. P. Salam, and G. Soyez, Eur. Phys. J. C **72**, 1896 (2012), arXiv:1111.6097 [hep-ph].

[47] G. P. Salam and G. Soyez, J. High Energy Phys. 0705 (2007) 086, arXiv:0704.0292 [hep-ph].

[48] Z. Bern, L. Dixon, and F. Febres Cordero, Private communication.

[49] A. Denner, S. Dittmaier, T. Kasprzik, and A. Muck, Private communication.

[50] G. P. Salam, Eur. Phys. J. C **67**, 637 (2010), arXiv:0906.1833 [hep-ph].

[51] L. Lyons, D. Gibaut, and P. Clifford, Nucl. Instrum. Meth. A **270**, 110 (1988).

[52] $\theta_{Z,jj}$ is defined as $\theta_{Z,jj} = \arccos \frac{(\vec{l}_1 \times \vec{l}_2)\cdot(\vec{j}_1 \times \vec{j}_2)}{|\vec{l}_1 \times \vec{l}_2||\vec{j}_1 \times \vec{j}_2|}$, where $\vec{l}$ and $\vec{j}$ are the momentum 3-vectors of leptons and jets.